APPLICATION OF THE TIGHT-BINDING ELECTRONIC STRUCTURE METHOD TO STUDY DEFECT FORMATION AND OPTICAL ABSORPTION IN COVALENTLY BONDED MATERIALS

BY

PURNIMA GHALE

THESIS

Submitted in partial fulfillment of the requirements
for the degree of Master of Science in Mechanical Engineering
in the Graduate College of the
University of Illinois at Urbana-Champaign, 2015

Urbana, Illinois

Adviser:

Professor Harley T. Johnson

ABSTRACT

Tight-binding or linear combination of atomic orbitals is a method for computing the electronic structure of materials. Like Density Functional Theory(DFT), it depends on the single electron approximation, but is significantly less expensive because it includes parameters from DFT, other ab-initio methods, and experiments. In terms of the system sizes usually studied in materials behavior computation, tight-binding bridges the distance and time domains between those typically covered by density functional theory (DFT) and classical molecular dynamics (MD) where the interactions between atoms are given by a pre-determined function, and the quantum mechanical nature of electrons is not accounted for.

In order to account for the quantum mechanical nature of electrons, the Schrodinger equation has to be solved for the electron wavefunction. The Schrodinger equation is a second order differential equation; one can think of it as a laplacian (∇^2) with inhomogeneities of the type $\frac{1}{|\mathbf{r}|}$ and other potentials, which themselves depend on the wavefunction (or charge density) and whose functional form is determined by several approximations. This is the problem solved by DFT, where in the ideal case, a complete continuous orthogonal basis set is used to solve the Schrodinger equation self-consistently. However, the basis set necessarily has to be discrete and finite, and convergence suffers because of the type and spatial extent of the inhomogeneity ($\frac{1}{r}$ type potentials).

For many materials, specially insulators and semiconductors, it is often more convenient to assume a basis set centered around atoms - i.e. by assuming that a bond is a perturbation of an atom[52], we can write the electronic wavefunction of real crystals in terms of atomic orbitals. We may then solve the DFT problem on a small system of atoms with this type of basis set, and obtain values of various interactions between orbitals of atoms. These values become parameters that can be used with tight-binding, and have the potential to scale the quantum mechanical treatment of electrons to computations involving hundreds of thousands of atoms. Traditionally, experimental results have also been used to determine parameters for tight-binding.

In this thesis, we present several applications of and extensions to the tight-binding method. After a brief description of the tight-binding method in chapter 1, we apply tight-binding to smaller, heterogeneous unit cells in chapters 2 and 3. In particular, we use tight-binding calculations as a part of total energy computation, and use it to get an insight into the kinetics of defect formation in chapter 2. Then in chapter 3, we compute the rates of optical absorption and individual atomic contributions to total absorption. Then in chapter 4, we present past work and our own developments that allow us to scale the applications in

chapters 2 and 3 to larger system sizes, where tight-binding as a method is most promising.

To my family.

ACKNOWLEDGMENTS

First of all, I would like to thank my advisor Professor Harley Johnson for introducing me to the tight-binding method and its application to heterogeneous materials and large scale computations, which also happens to be the topic of this thesis. I am also grateful for the opportunity to work with him, and learn from him by observation, how to do research - how to identify and ask critical questions, which gaps in knowledge to pursue, and how to communicate more effectively. In short, I could not write this thesis without his guidance, encouragement and mentorship.

In addition, I would also like to thank professors in classes whose ideas have shaped my research. In particular, I would like to thank Professor Shinsei Ryu (quantum mechanics), Professor Taylor Hughes(solid state physics), Professors Elif Ertekin and Petros Sofronis (solid mechanics), and Professor Parviz Moin (perturbation theory). I am also grateful to Professor Jonathan Freund and the XPACC group for support and community. Furthermore, my thesis would also not have been possible without the amazing competence of Kathy Smith and Katrina Hagler.

I would also like to acknowledge my parents for their unshakeable trust and confidence in me, and my siblings for being the source of long-running-series of bad jokes and much needed distraction. I thank my labmates for their friendship, problem-solving, and patience in hearing my rants. I also want to extend many thanks to my commiserating friends outside of lab, without whom life as a graduate student would be very uneventful.

This is only the master's thesis, and I hope to continue and finish my phD dissertation, so onwards and upwards!

Part of the work was done with funding from (Department of Energy, National Nuclear Security Administration, Award Number DE-NA0002374).

TABLE OF CONTENTS

CHAPTER 1

ELECTRONIC STRUCTURE

Recent advances in computing power have made calculations of material properties using quantum mechanics more feasible. The basis of a quantum mechanical calculation starts with the Schrodinger equation that contains a full description of the system - all electrons and all nuclei within the atom are represented in the Schrodinger equation. Using this equation, we may want to determine the total energy of the system, or how a system evolves in time. The time-dependent Schrodinger equation is as follows:

$$i\hbar\frac{d\psi(\mathbf{r},t)}{dt} = \hat{H}\psi(\mathbf{r},t) \tag{1.1}$$

On the right hand side, $\hat{H}$ is the Hamiltonian, and it behaves as any other linear operator - it can be a function, derivative, or constant multiplication, and the solution $\psi(\mathbf{r},t)$ is the wavefunction - a multi-dimensional function that completely defines the state of the system. If $\hat{H}$ does not depend directly on time t, the above equation is separable in $\{\mathbf{r_i}\}$ and t, in which case, our main concern is to solve the stationary, time-independent Schrodinger equation:

$$\hat{H}\psi_k = \lambda_k\psi_k \tag{1.2}$$

The above equation is now an eigenvalue problem where the eigenvalues λ are the possible energy states of the system. Each eigensolution, or stationary state, evolves in time as

$$\psi_k(\{\mathbf{r}\},t) = \psi_k(0)e^{-\frac{i}{\hbar}\lambda_k t} \tag{1.3}$$

We now shift our focus to the dermination of the Hamiltonian. The Hamiltonian of a system reflects the total kinetic and potential energies of the system, therefore it depends on what particles are included in the system, and their interactions with one another. The Schrodinger equation that includes all kinetic and potential energies of the particles in the system, and the interations between them, takes the following form [38]:

$$\frac{-\hbar^2}{2m_e}\sum_{i=1}^{N}\nabla_i^2\Psi + \sum_{i<j}^{L}\frac{e^2}{|\mathbf{r_i}-\mathbf{r_j}|}\Psi - \sum_{i,I}\frac{Z_I e^2}{|\mathbf{r_i}-\mathbf{R_I}|}\Psi + \sum_{I<J}\frac{Z_I Z_J e^2}{|\mathbf{R_J}-\mathbf{R_I}|}\Psi + \frac{-\hbar^2}{2M}\sum_{I=1}^{L}\nabla_I^2\Psi = E\Psi \tag{1.4}$$

Here, the lowercase indices i, j are for electrons and the uppercase indices I, J account for nuclei; e

represents electronic charge, whereas $Z_I e$ represents the nuclear charge in atom I. The first operator ∇_i^2 and the last ∇_I^2 are the kinetic energy operators for every electron and nucleus respectively. The second term $\frac{e^2}{|\mathbf{r_i}-\mathbf{r_j}|}$ accounts for the interaction between electrons. The third term represents the interaction between the nuclei and every electron, followed by the term that accounts for interaction between atomic cores. On the right hand side, E is the energy of the system. The wavefunction $\psi(r_1, r_2, ..r_N, R_1, R_2, ...R_M)$ contains all the information about the state of the system, and to find any material property, known as an observable in quantum mechanics, we need the wavefunction. The details of representing operators as matrices, and other information are presented in the first appendix A.

As it is, equation 1.4 is intractable because of the many-dimensionality of the problem, and the complete wavefunction is almost never known. The full problem is not solved unless by Monte-Carlo methods that are capable of accurately integrating over many degrees of freedom. These multidimensional spatial integrals are behind Quantum Monte Carlo; these methods are accurate but do not scale computationally with system size.

The above problem of multidimensionality can be simplified by two approximations so that only relevant and computationally feasible parts of the calculation are done. For a general history of various electronic structure methods, see [38], for Density Functional Theory, and the bigger context of which our tight-binding presentation is just one type, see [12] [28] [29] [47]. Here, we briefly outline the two major approximations:

1. Born Oppenheimer approximation: separate the electronic structure from nuclear motion. $\Psi(r, R) = \psi(r)\phi(R)$ where $\psi(r)$ is the electronic part of the wavefunction. This is possible because electrons are much lighter than nuclei so we can assume that the last term in the above equation is negligible and the nucleus-nucleus interaction V_{I-I} is a constant that is only a function of the distance between the nuclei themselves. This gives the equation:

$$\frac{-\hbar^2}{2m_e}\sum_{i=1}^{N}\nabla_i^2\psi + \sum_{i<j}^{L}\frac{e^2}{|\mathbf{r_i}-\mathbf{r_j}|}\psi - \sum_{i,I}\frac{Z_I e^2}{|\mathbf{r_i}-\mathbf{R_I}|}\psi + V_{I-I}\psi = E\psi \tag{1.5}$$

2. Single electron approximation: instead of adding over all the kinetic energies and the interaction between electrons, we assume that they can be represented by an external potential $V_{ext} = \frac{Ze^2}{|\mathbf{r}-\mathbf{R}|} + V_{xc}$:

$$\left(-\frac{\hbar^2}{2m}\nabla^2 + V_{ext}\right)\psi(r) = \hat{H}\psi(r) = E\psi(r) \tag{1.6}$$

   This is the Kohn-Sham equation, and the beginning of the single electron approximation. Here, the complications of going from a many electron wavefunction $\psi(r_1, r_2, ..)$ to a single electron wavefunction $\psi(r)$ are included in the exchange-correlation potential V_{xc}.

This thesis describes work done using the tight-binding method which is built on the foundations of the two approximations mentioned above. Furthermore, if the system is periodic or has discrete translation

symmetries, then one can take advantage of periodicity to calculate the properties of the exact system in bulk. This approach works very well with pure bulk systems, but not for systems with defects or inhomogeneity, systems which are of primary interest in materials science and engineering. We will now proceed to describe tight-binding as one specific electronic structure method.

1.1 Introduction to tight-binding formulation

Tight-binding or Linear Combination of Atomic Orbitals (LCAO) is a semi-empirical method that contains fitting parameters as well as purely ab-initio calculations. The basic premise of the LCAO method is that the single electron wavefunction can be approximated by a suitable linear combination of orbitals[56]. The advantage of tight-binding approach is that with a few parameters, it accounts for the quantum mechanical nature of the electrons, while scaling relatively well with system size. Tight-binding parameters were first computed to study the bulk properties of materials, such as the band structure of periodic covalent crystals like silicon and other zinc-blende structrues [7] [20] [60]. Tight-binding however, can also be used for large, heterogeneous crystal structures, which is how it will be used in this thesis. There are books [20] [45] [57] and papers [6] [13] [21] [22] [55] [56] on the description of this method, and its implementation for large scale structures. Even more references exist on the underlying quantum physics used in these methods [3] [17] [33]. In this chapter, we introduce basic information that a newcomer in the field should know in order to set up and run a tight-binding calculation. The construction of a suitable Hamiltonian matrix, and its diagonalization for eigensolutions (or the alternatives to diagonalization) are two major components of a tight-binding computation.

1.2 Setup

To start with, we consider the simplest case, a single atom with one electron - hydrogen. From quantum mechanics ([17] [33]), we know that the electron wavefunction depends the Schrodinger equation:

$$-\frac{\hbar^2}{2m}\nabla^2\phi + V\phi = E\phi \tag{1.7}$$

where V is the external potential. In the case of hydrogen, and other atoms, the Hamiltonian is $H = -\frac{\hbar^2}{2m}\nabla^2 - \frac{Ze^2}{|\mathbf{r}-\mathbf{R}|}$ where $\mathbf{r}$ and $\mathbf{R}$ are the coordinates of the electron and the nuclei respectively. The wavefunctions obtained are the well-known s,p,d,f atomic orbitals, sometimes written as $|nlm\rangle$, where n is the orbital number, l is the angular momentum, and m is the angular momentum in z-direction. Electron spin is not included yet in our discussion but can be included by adding a spin-orbit coupling term. For more details see [17] or [33].

Now, let us consider two hydrogen atoms at positions $\mathbf{R_m}$ and $\mathbf{R_n}$, separated by distance d_{mn} . The

Hamiltonian for electrons is given by [22] :

$$H_{total} = -\frac{\hbar^2}{2m}\nabla^2 - \frac{Z_m e^2}{|\mathbf{r} - \mathbf{R_m}|} - \frac{Z_n e^2}{|\mathbf{r} - \mathbf{R_n}|} \tag{1.8}$$

Here, the interaction between nuclei are ignored, as their potential energy can be modeled as classical

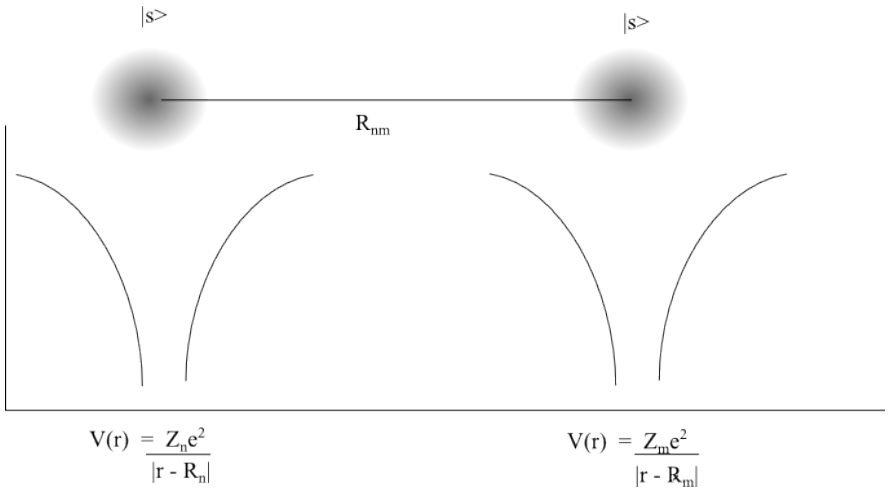

Figure 1.1: Isolated identical atoms, with one valence electron in the s-orbital. Since they are far apart, their potentials and wavefunctions do not interact. The Hamiltonian is diagonal.

Coulomb potentials, and it introduces a shift in the diagonal elements. When they are separated $R_{nm} \to \infty$, the two atoms do not interact. So, the total Hamiltonian matrix is diagonal such that:

$$\langle \phi_n | H_{total} | \phi_m \rangle = E_s \delta_{nm} \tag{1.9}$$

Here, and later, the $|\phi_m\rangle$ and $\langle \phi_n|$ are the atomic orbitals and their complex conjugates respectively. The total wavefunction is written as a linear combination of these orbitals, more details of which are provided in appendix A.

1.3 Bonding and anti-bonding

When the atoms are brought closer, the interaction between the nucleus at $\mathbf{R_m}$ and $\phi_n(\mathbf{r} - \mathbf{R_n})$, the orbital belonging to atom at $\mathbf{R_n}$, is non-zero. In that case, the Hamiltonian is no longer diagonal, and is written as:

$$H = \begin{bmatrix} E_s & V_{12} \\ V_{21} & E_s \end{bmatrix} \tag{1.10}$$

Diagonalizing this Hamiltonian, the degeneracy is lifted, i.e. previously there existed two states with the same energy E_s but when they interact, two distinct energy levels appear. The lower energy level is called

the bonding energy level, and the higher energy value corresponds to the anti-bonding level.

$$\psi_{bonding} = \frac{1}{\sqrt{2}}\left(\phi_s^A + \phi_s^B\right) \tag{1.11a}$$

$$\psi_{anti-bonding} = \frac{1}{\sqrt{2}}\left(\phi_s^A - \phi_s^B\right) \tag{1.11b}$$

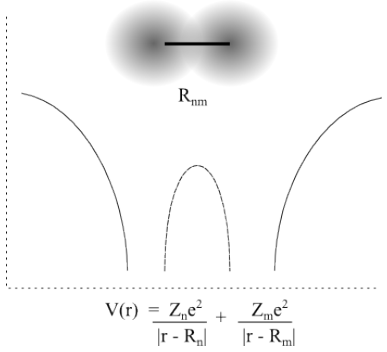

(a) At closer interatomic distances, the electron wavefunction is affected by the electric potential of another nuclei.

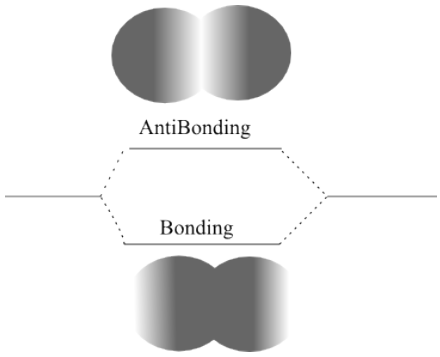

(b) Formation of molecular wavefunction and separation of bonding and anti-bonding energy levels

Figure 1.2: Bonding and anti-bonding energy levels are formed when atoms are close enough to interact.

In figure 1.2, the electron-density distributions are presented for bonding and anti-bonding levels of our toy problem. The lower energy level, labeled bonding, is darker between the atom cores, showing higher electron density as a result of the symmetric sum in equation 1.11a. On the other hand, the anti-bonding energy level, shows almost no electron density between the atoms, with highest electron density(darker) on the outside. This is because the anti-bonding state is an antisymmetric sum shown in equation 1.11b and has higher energy than the bonding state.

1.4 Periodic crystals

We extend our discussion of bonding and anti-bonding orbitals to include periodic crystals, in the simplest, 1-dimensional form. In figure 1.3, an infinite chain of atoms is presented. Each atom now contributes one valence electron, and one energy level. Because each atom is still identical, the degeneracy (an infinite number of atoms with the same energy) is broken when these atoms interact with one another, but instead of obtaining two discrete bonding and anti-bonding energy levels, we obtain valence and conduction bands respectively.

Numerically, it is impossible to study bulk crystals by arranging an infinite array of atoms, so the next step is to use the periodic nature of the above setup, by defining a crystal structure. A crystal structure is uniquely defined by two quantities (a) the unit cell - the repeating configuration of atoms and bonds, and (b) the lattice - how the repeating unit cells are arranged in space, this arrangement is defined using lattice

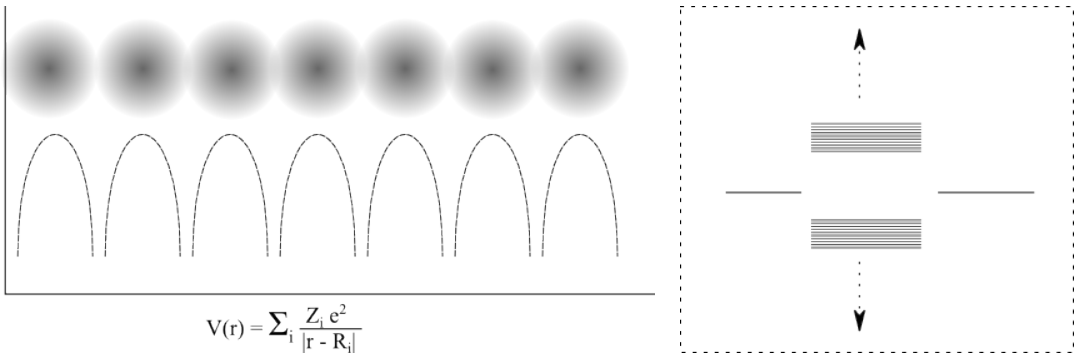

(a) An infinite chain of atoms bonded in 1-D

(b) Bonding and anti-bonding bands

Figure 1.3: An infinite chain of atoms in real space implies that the bandstructure in reciprocal space will be continuous. Here, each atom contributes one valence electron, forming two bands. For an infinite chain of carbon atoms, contributing four valence electrons, $4 \times 2 = 8$ bands are observed.

constants, and displacement vectors.

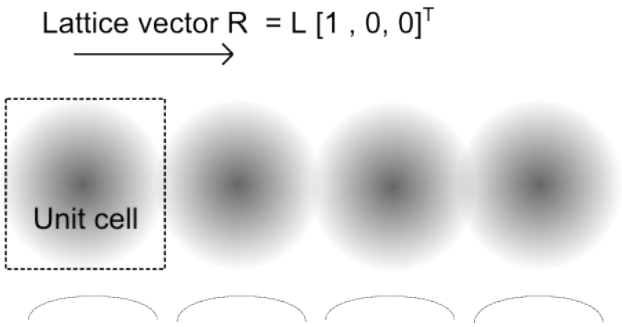

Figure 1.4: Unit cell and lattice vector shown. This periodicity means that $\mathbf{x} = \mathbf{y} + n \cdot \mathbf{R}$, where $\mathbf{y}$ is the coordinate system inside one unit cell $\mathbf{y} \in [0, L]$. For now, we assume that the periodic potential due to the nuclei $V = -\frac{Ze^2}{|\mathbf{r}-\mathbf{R_n}|}$ is very small.

In the one-dimensional case discussed above, the unit cell contains one atom, and is periodic by length L, in the x-direction. We therefore have a definition of the crystal structure, and can now study the infinite chain of atoms, with knowledge only of the unit cell (which contains only one atom here), and the lattice vector. Specifically, the wavefunction of such a system, $\psi(x)$, will have to satisfy:

$$\psi(0) = \psi(L) \tag{1.12a}$$

$$\left.\frac{d\psi}{dx}\right|_{x=0} = \left.\frac{d\psi}{dx}\right|_{x=L} \tag{1.12b}$$

Here the position ($\mathbf{x}$) in space can be decomposed into two parts $\mathbf{x} = \mathbf{y} + n\mathbf{R}$, where $\mathbf{y}$ is the coordinate position inside the unit cell, and $\mathbf{R}$ is the vector that determines how those unit cells are arranged in a periodic lattice. The next step is to separate the wavefunction into parts dependent on $\mathbf{y}$, and $\mathbf{R}$

$$\psi(\mathbf{x}) = \phi(\mathbf{y})e^{i\mathbf{G}\cdot\mathbf{R}n} \tag{1.12c}$$

In one dimension,

$$e^{iGx} = e^{iG(x+nL)} = e^{iGx}e^{iGnL} \tag{1.12d}$$

$$GnL = 2n\pi \tag{1.12e}$$

Here $G = \frac{2n\pi}{L}$, where n is any integer. A useful representation of the physics of the crystal, is via the bandstructure, represented by a plot of the energy vs. k, as seen in figure 1.5. For a free electron, $E = \frac{\hbar^2 k^2}{2m}$, and the bandstructure is a parabola. Periodicity, however, limits the values of k that are unique since $\mathbf{k}$ and $\mathbf{k} + \mathbf{G}$ are equivalent due to periodicity. The equivalent of a unit cell, in the reciprocal (k-)space is the Brillouin zone. Instead of plotting all plane waves e^{ikx} for $k \in [-\infty, +\infty]$, the first Brillouin zone $k \in [-\frac{\pi}{L}, +\frac{\pi}{L}]$ can be used to represent all the physics of infinitely extended crystals. This simple periodicity, determined by the lattice constant or periodicity vector $\mathbf{R}$, results in the bandstructure shown in black in figure 1.5.

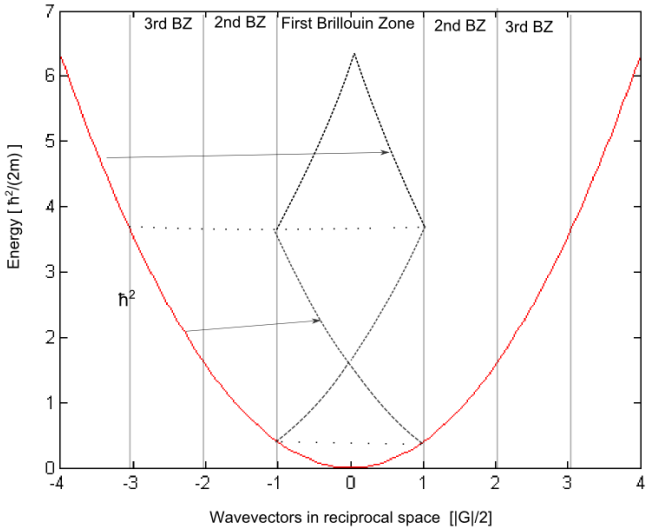

Figure 1.5: Bandstructure formation in 1-D when the periodic atomic potential is zero. Because of the periodicity of the 1-D lattice, all details of the electronic structure can be represented by the first Brillouin zone. Note how parts of the $energy = \frac{\hbar^2 k^2}{2m}$ parabola (the red curve between dotted horizontal lines) can be translated by units of G so that the possible values of wavevector k remain inside $[-G/2, +G/2]$.

The addition of the nuclear potential, and interaction with other electrons, which are weaker than nucleus-electron interactions, add detail to the bandstructure. Specifically, the addition of the nuclear potential changes the curvature of the bandstructure at the $k = 0$ and $k = \pm\frac{G}{2}$ points. This is manifest in two observed quantities: (a) in real crystals, we observe an effective mass of an electron in a crystal, which determines transport. The effective mass is given by:

$$m^* = \left. \frac{1}{-\frac{\partial^2 E}{\partial k^2}} \right|_{k=0} \tag{1.13}$$

and (b) the bandgap – this is the difference in energy between the highest occupied energy level (valence) and the lowest empty energy level (conduction) bands. In figure 1.6, when atomic potentials are included, they affect the values of energy $E = \frac{\hbar^2 k^2}{2m} + V(r)$. As a result, the bands separate at band edges ($k = 0$ and $k = \pm\frac{G}{2}$). Also, the unit cell we considered has one valence electron, which implies that only one band, the lowest, will be filled. This leads to a band-gap at $k = \pm\frac{G}{2}$. For example, if each unit cell contributed two

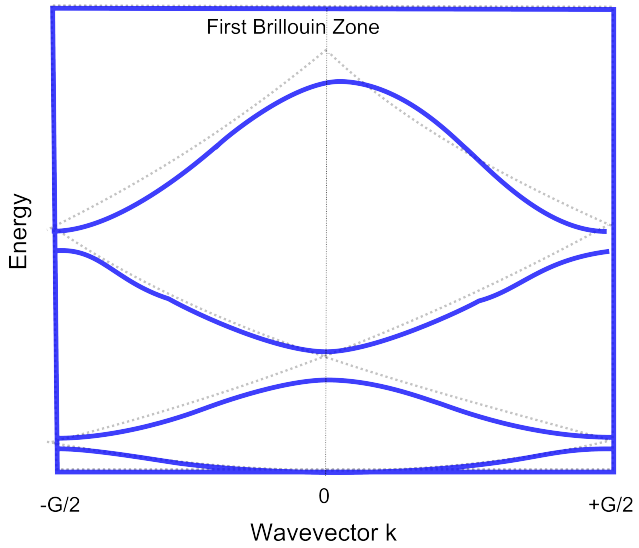

Figure 1.6: Addition of the atomic potential changes the dispersion (energy-vs.-k) relation, which can result in gaps at the $\Gamma-$point, or at the band edges $\mathbf{k} = \pm\frac{\mathbf{G}}{2}$ for the one-dimensional case.

valence electrons, arranged in the same one-dimensional set up, then two bands would be filled, leading to a bandgap at $k = 0$. The value of the bandgap is the difference in energy between the highest occupied energy level (valence band), and the lowest unoccupied energy level (conduction band). This also determines the effective electron mass, since it is defined at $k = 0$ – i.e. the valence band effective mass may be different from the conduction band effective mass of the electron. All of this is determined by the bandstructure in pure crystals. This is of course a simplified description of the bandstructure, and more details can be found in [3].

1.4.1 Heterogeneous materials

Often when computing the electronic structure of real, heterogeneous materials, we cannot take advantage of the periodicity of the system. Nor can we assume that the electrons behave as free electrons with an effective mass. For example, the system under study may be an array of quantum dots, where each unit cell is composed of thousands of atoms. In this case, we can assume that the reciprocal brillouin zone $G \to 0$, and the $k = 0$ or $\Gamma - point$ computations will be enough to resolve most of the physics of the system. In this context, the density of states, which counts the number of states at a given energy value E, will be the

quantity of interest, and can be represented as:

$$dos(E) = \frac{1}{D}\sum_i \delta(E - E_i) \tag{1.14}$$

Together with the Fermi-Dirac distribution,

$$f(E) = \frac{1}{1 + \exp\left[\frac{E-\mu}{k_B T}\right]} \tag{1.15a}$$

that satisfies the equation

$$N_{electrons} = \int_{E_{min}}^{E_{max}} f(E)dos(E)dE \tag{1.15b}$$

the local density of states can be used to compute total electronic contribution to energy:

$$\langle E\rangle = \int_{E_{min}}^{E_{max}} Ef(E)dos(E)dE \tag{1.15c}$$

and other quantities. For example, generally, an observable q can be written as:

$$\langle q\rangle = \sum_i \langle\psi_i|\hat{q}|\psi_i\rangle\, f(E_i) \tag{1.15d}$$

In terms of the density of states, for large heterogeneous systems, it is usually represented in the following form:

$$\langle q\rangle = \int_{E_{min}}^{E_{max}} q(E)f(E)dos(E)dE \tag{1.15e}$$

In this chapter, we introduced some of the physical concepts required for electronic structure calculations, and the approximations made to get there. In chapter 2, we use tight-binding calculations as a part of total energy computation. We note that because of the Born-Oppenheimer approximation, electrons are treated quantum mechanically, while nuclei are treated as classical objects. This type of total energy calculation is then used to determine whether certain types of defects can be formed in graphene and similar carbon-based materials. Transferability of the tight-binding parameters is a necessary condition for the validity of calculations. In this context, the limitations of the method compared with ab-initio calculations are presented.

In chapter 3, we make further use of electronic structure methods to study the optical behavior of carbon-based materials such as graphene sheets and nanotubes. A commonly used and simple expression for optical absorption and emission rates within the independent electron approximation is derived. This is modified using projection methods to resolve absorption and emission atomically.

In chapter 4, we will look at larger heterogeneous systems containing tens of thousands of atoms, where tight-binding as a method is most effective. There, methods will be presented that do not require di-

agonalization of the Hamiltonian in order to compute observables. Although many O(N) alternatives to diagonalization exist, we focus on Chebyshev expansion techniques because polynomial expansion is easy to understand, simple to implement, and allows for error analysis in a simple way.

CHAPTER 2

GRAPHENE: DEFECT FORMATION AND FUNCTIONALIZATION

2.1 Structure of graphene and carbon nanotubes

Graphene is one of the allotropes of carbon, but it is different in that it is a 2-dimensional, highly covalent structure. Historically, the crystal structures of diamond and graphite, formed from the same element, have been of interest; the band-gap of graphite was being studied as early as the 1950s [40] [60]. Graphite is a 3-dimensional crystal with strong covalent bonding on one plane, and weak van-der-waals bonding perpendicular to these planes. In other words, a graphite crystal is a stack of graphene lattices connected by van-der-waals forces. Graphene was first manufactured in 2004 [44], and since then interest in graphene has been driven by its use as an experimental setup to study physics in 2-dimensions, and for its unique material properties such as its high strength and electrical conductivity. More recently, its optical absorption properties were also of interest for applications in electrodes and dye-sensitized solar cells [61].

The graphene structure is made up of two repeating atoms, belonging to two different bravais lattices, arranged to form a honeycomb structure on a single plane. A schematic of the unit cell of graphene, and its lattice vectors in 2-dimensions are shown in figure 2.1. Each carbon atom is $\sigma-$ bonded to three carbon atoms, and a delocalized $\pi-$electron-cloud also connects a carbon atom with all other atoms in the structure. The 2-dimensionality of graphene gives unique properties to the valence/conduction electrons, which explains its very high conductivity, and the $\pi-$bondedness is responsible for its incredible strength [43] [44] . These 2-dimensional graphene sheets can also appear in "rolled-up" form as carbon nanotubes, which are cylindrical one-dimensional structures. The properties of carbon nanotubes depend on the way they are terminated at the edges, the arrangement of carbon atoms at the boundaries, and the chiral angle. Depending on this structure, a carbon nanotube can be metallic, semi-metallic or even insulating. These nanotubes therefore offer immense potential for material engineering. The strength of nanotubes can also create challenges since one has to be able to create nantoubes at the right termination to control conductivity, for use in circuits, for example. A very high electric field is often required to break a pure carbon nanotube with atomic precision, and Scanning Tunneling Microscopes (STMs) are used for this purpose [1]. In the process of cutting a carbon nanotube via STM, the formation of a local 5-7-7-5 defect, also known as a Stone-Wales defect, is frequently observed; a Stone-Wales defect is formed when one carbon-carbon bond is rotated by 90-degrees to create two heptagonal and pentagonal structures in place of the four undisturbed hexagons. The formation of these

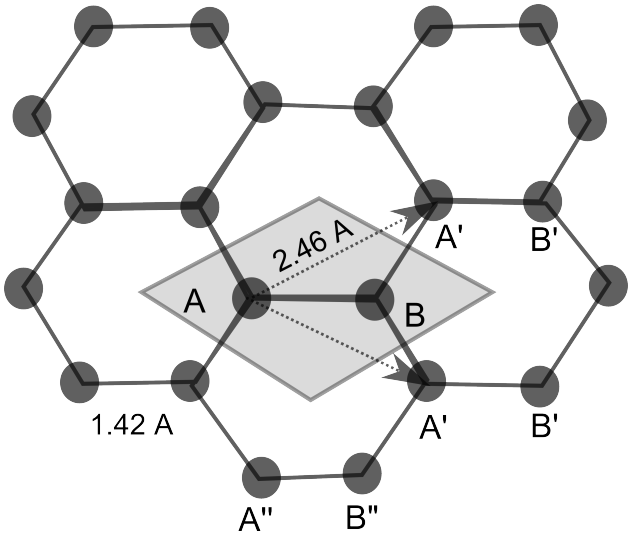

Figure 2.1: Crystal structure of graphene. The unit cell (shaded) contains two carbon atoms, separated by 1.42 Angstroms. The lattice vectors are of length 2.46 Angstrom, and replicate the unit cell to create the structure of graphene. Figure reproduced from [60]

Stone-Wales defects will be the focus of this chapter.

Furthermore, the process of defect formation may be facilitated by local chemical alterations such as hydrogen adsorption [5] on graphene. This process of introducing a functional group, or dopant in graphene, has been used for band gap engineering in nanoribbons[18], to tune bandgaps in graphene [14] , to modify electronic and magnetic properties[66], and other properties[11] [25] [34]. In this chapter, we investigate the effect of surface functionalization on the formation of a 5-7-7-5 defect. Since the creation of a local Stone-Wales defect includes change in chemical bonding, we calculate the energies associated with the formation of, and possible pathways between, stable initial (perfect graphene or nanotubes) and meta-stable final (structures with a Stone Wales defect) atomic configurations. To accomplish this, we extend our previous discussion of electronic tight-binding calculations to compute total energies, and apply a genetic minimization heuristic to approximate the best pathway for defect formation. We repeat equivalent reaction pathway computations for defect formation with and without surface functionalization in graphene and one type of carbon nanotube. We conclude that surface functionalization indeed increases the chance of defect formation in 2-dimensional graphene, however, no effect was observed in the carbon nanotube.

2.2 Total energy calculation

In chapter 1, the tight-binding description provided information about the bandstructure and electronic contributions to the total energy of the system. In this chapter, we extend that description by adding the contributions due to atom-core interactions. The total energy is given by [21] [47]:

$$E = E_{valence} + E_{core} \tag{2.1}$$

where $E_{valence}$ is a measure of the energy due to electronic bonding, and is calculated using tight-binding, and E_{core} is the core atom contributions. The electronic contribution to the total energy is computed using the eigenvalues of the tight-binding Hamiltonian. The matrix elements of the tight-binding Hamiltonian are given by:

$$\mathbb{H}_{\alpha,\beta} = t_{\alpha,\beta}(r) + \epsilon_\alpha \delta_{\alpha,\beta} \tag{2.2}$$

where the indices α, β represent the basis orbitals used, $t_{\alpha,\beta}$ are the tight-binding parameters associated with bonding between two orbitals that depend on the type of crystal, atom-types, and on the distance between the orbitals (r), ϵ_α is the energy of the orbital, present even when there is no bonding, such as ϵ_s or ϵ_{px} and contributes to the diagonal of the Hamiltonian, which is represented by $\delta_{\alpha,\beta}$. Using the parameterization from [62]:

$$t_{\alpha,\beta}(r) = t_{\alpha,\beta}(r_0) \left(\frac{r_0}{r}\right)^{n_a} \exp\left[-n_b \left(\frac{r}{r_t}\right)^{n_c} + n_b \left(\frac{r_0}{r_t}\right)^{n_c}\right] \tag{2.3}$$

where the strength of interaction between two orbitals α and β on two different atoms separated by distance r is given in terms of $t_{\alpha,\beta}(r_0)$, the strength of interaction between orbitals at the equillibrium bond length, r_0 is the equillibrium bond length, r_t is the cutoff parameter, and the other parameters n_a,n_b and n_c give the appropriate power-law behavior. The eigenvalues of the Hamiltonian in equation 2.2, E_i are then used to compute the electron-contribution to total energy as follows.

$$E_{valence} = \sum_i E_i f_i - \sum_\alpha E_\alpha \tag{2.4}$$

Here

$$f_i = \frac{1}{1 + \exp\left[\frac{E_i - \mu}{k_B T}\right]}$$

represents the Fermi-Dirac statistics of electrons at various energy levels, and E_α is the energy contribution if there is no bonding. The next step of the calculation is to include the effect of interaction between atom-cores. This is included by using the following expression:

$$E_{core}(r) = E_{core}(r_0) \left(\frac{r_0}{r}\right)^{m_a} \exp\left[-m_b \left(\frac{r}{r_c}\right)^{m_c} + m_b \left(\frac{r_0}{r_c}\right)^{m_c}\right] \tag{2.5}$$

In the above parameterization, which is complementary to the parameterization in equation 2.3, r_c is the cutoff distance for interactions between atomic cores, and r_t is the cutoff for the tight-binding Hamiltonian. They are often assigned the same value, but letting them vary gives greater flexibility in parameterization across multiple properties. r_0 is the equillibrium distance, at which band structure and total energies are calculated. Other constants in equations 2.3 and 2.5 are parameters that depend on the tight-binding parameterization. Other tight-binding parameters for carbon exist for specific application type [35] [46] [47]. Our choice was made on the basis of requiring an orthogonal tight-binding basis set that also included

hydrogen-carbon interactions.

2.3 Determination of the best reaction pathway

2.3.1 Reaction pathway

Now that the total energy of a given atomic configuration can be calculated, the obejctive is to look at the kinetics of Stone-Wales defect formation.

The reaction pathway is a sequence of chemical and atomic configurational changes that take place from the initial to the final structure; here, the initial structure is the perfect graphene unit cell, and the final structure is the same unit cell with a 5-7-7-5 defect formed. Each configuration of atoms, which represents a step in the reaction pathway, has an energy associated with it, given by equation 2.1 and explained in section 2.2. To determine the thermodynamic probability of a reaction, the Arrhenius factor of the form

$$\text{Rate} \propto \exp\left[-\frac{\Delta E}{k_B T}\right] \tag{2.6}$$

is useful, where ΔE represents the activation energy of a reaction, k_B is the Boltzmann constant, and T is the temperature.

The activation energy is the difference between the maximum and minimum energy configurations in the reaction pathway. A lower activation energy signifies higher probability of defect formation, which in turn facilitates manipulation of carbon nanotubes via STM. Our objective in this section is to outline a heuristic to determine the reaction pathway that has the minimum activation energy. These most feasible reaction pathways are called minimum energy pathways.

In general, minimum energy pathway methods depend on force computations using the Hellman-Feynman theorem[27] [55]. However, the analytic computation of gradients requires a converged self-consistent-charge electronic structure, and a way to handle non-orthogonality [12] [15]. With the tight-binding parameters used, these two conditions are computationally expensive since each self-consistent charge computation is an iterative loop of matrix diagonalizations, and calculating the gradient numerically with respect to every atom position would also be expensive for highly multi-dimensional problems containing more than a few atoms. Therefore, gradient-based methods will be avoided in favor of gradient-free methods of optimization since we can calculate the total energy for various atomic configurations in a relatively inexpensive way.

2.3.2 Description of genetic minimization algorithm

Gradient based methods such as the nudged-elastic-band[26] and those based on finding stationary transition-states[36] [42] exist, but will not be used here due to our constraints in gradient computation mentioned in

previous section. Furthermore, for problems with many degrees of freedom, gradient-free optimization [10] is preferred, of which genetic algorithms [16] are just one type.

Here, we follow [2] and develop a general genetic heuristic to obtain the nearest minimum path. The method is quite robust in that the optimized structures in the reaction pathway are reproducible with slightly varying initial estimates, and different initial population sizes.

First, we present a simple genetic heuristic that describes how one might obtain the minimum energy unit cell from an initial estimate, which is one step of the reaction pathway. With a slight modification, the same heuristic is applied to obtain the minimum activation energy pathways. The pseudo code for geometry optimization is as follows:

1. Propose an estimated optimal structure.
2. Create a population of structures by adding random deviations drawn from a normal distribution with $\sigma = 0.1$ Angstroms variation. Also add random deviations from distributions with $\sigma = 0.2$ and $\sigma = 0.3$.
3. Iterate the following until convergence
   (a) Choose M structures that are of the lowest energy. Call this the parent population.
   (b) Take linear combinations of every structure in the parent population. Call this the child population.
   (c) Select minimum energies from the parent and child populations.
   (d) Mutate: add random noise with a small probability.
   (e) Converge when the standard deviation in the minimum population $\leq$ threshold value.

2.3.3 Application

To obtain the minimum energy pathway, start with an estimate of the reaction process. For this, it is necessary to have a predetermined number of chemical configurations (steps) between the initial and final configurations. Suppose this path is a linear interpolation between the initial and final chemical structures.Then, deviations to this pathway were added in various magnitudes, while the initial and final chemical structures stay the same. The genetic evolution algorithm goes through the initial population and optimizes to the nearest reaction pathway with the minimum activation energy, i.e. the local minimum. Detailed results of one such simulation are shown in figure 2.2. In figure 2.2(a), all proposed reaction pathways and their corresponding energies at the begining of genetic selection, are presented. As expected, these initial proposed paths vary widely in their energy profile and activation energy. At each iteration of selection, figure 2.2(b) shows the average activation energy in the proposed paths. We observe that within 25 iterations, the activation energy for a proposed minimum energy path between the initial and final structures have decreased by more than 10 eV. Furthermore, the optimization algorithm stops when all proposed paths converge to the

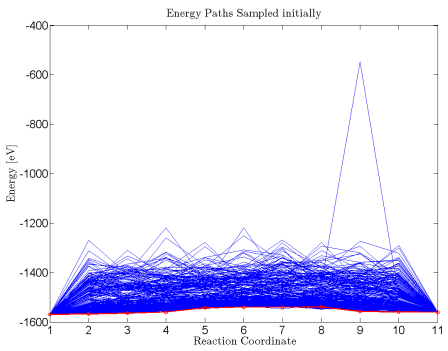

(a) The paths and corresponding energies sampled by the genetic algorithm.

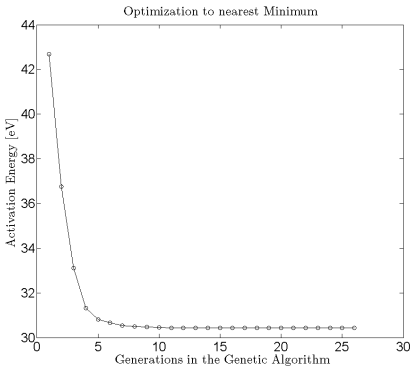

(b) The activation energy converges to the nearest minimum.

Figure 2.2: Figure (a) shows the initial set of paths sampled in first generation of the genetic algorithm (in blue), and the final path accepted (in red) after several iterations. In figure (b), the average activation energy of all paths in each generation is calculated.

minimum solution within a pre-determined tolerance, i.e. when the activation energies of the paths have a standard deviation of $\leq 1 \times 10^{-3}$ eV.

2.4 Stone-Wales defect formation

Having established convergence to the nearest minimum energy pathway in section 2.3, the above set of methods are used to investigate Stone-Wales defect formation in a 50-atom graphene unit cell with periodic boundary conditions, shown in figure 2.3. We attempt to rotate the bond at the center of this unit cell by 90 degrees in clockwise and anticlockwise directions.

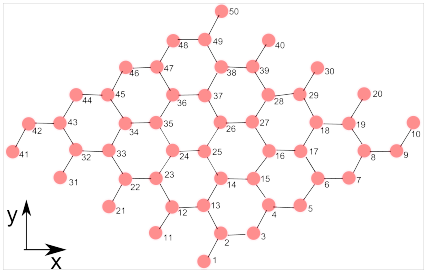

(a) Setup of the planar perfect graphene sheet with no defect.

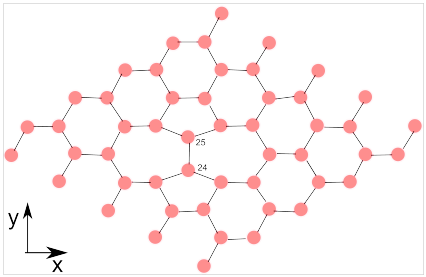

(b) A Stone-Wales defect on the planar graphene sheet

Figure 2.3: The initial and final states for a reaction pathway. The Stone Wales defect shown in figure (b) is constructed by a bond rotation in counter-clockwise direction.

In the clockwise and anticlockwise bond rotation, all proposed paths connecting the initial and final states are evaluated through the iterative genetic optimizer until convergence. The results for defect formation are presented in figure 2.4. Absent any other chemical defects, or different terminations at the edges, both bond rotations are chemically equivalent, and this is evident in the energies associated with the reaction pathway, shown in figure 2.4. We include the bond rotation difference here to point out that in the presence

of non-uniform surface functionalization, the two types of 90-degree bond rotations will not be equivalent in general.

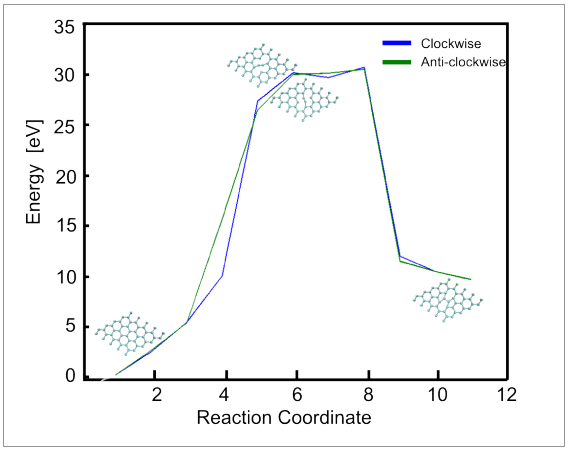

Figure 2.4: The optimized energy paths of Stone-Wales Defect formation. The direction of the bond rotation has no effect on the energy barrier of this reaction.

2.5 Effect of hydrogen adsorption on graphene

It is known that hydrogenation can be used to tune various electronic, magnetic and chemical properties, listed in the beginning of the chapter. In this section, the effect of functionalization on Stone-Wales defect formation is studied by using hydrogen as a simple model of an adsorbed functional group. We begin by determining the minimum energy configuration for hydrogen adsorption.

2.5.1 Setup: adsorption of atomic hydrogen on graphene surface

The best position for hydrogen-adsorption is determined by sampling different (x,y,z) coordinates, and finding the minimum energy configuration. The graphene unit cell is held constant, a hydrogen atom is added at various positions on its surface, and the energy of the system is computed with methods outlined in sections above. According to our results, shown in figure 2.5b, the best position for hydrogen adsorption is 0.9 Angstroms above the surface of that unit cell, and at an interstitial position in the hexagonal structure.

2.5.2 Reaction pathways, in case of hydrogenated unit cells

Next, we calculate the activation energy of Stone-Wales defect formation in these graphene-like unit cells with hydrogen adsorbed in the position shown in section 2.5.1. We compute the reaction pathways when the bond under consideration is rotated in the clockwise and anticlockwise directions, and compare these pathways to the results in section 2.4 where no atomic hydrogen was adsorbed. The results are shown in

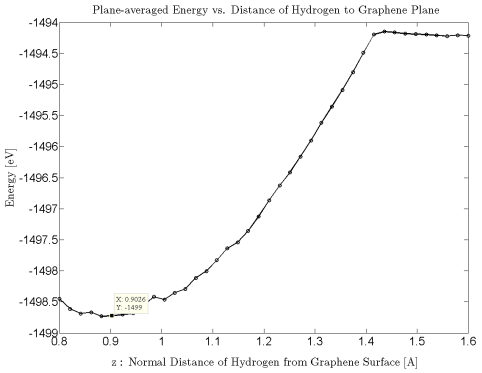

(a) Determining the preferred height for hydrogen atom adsorption.

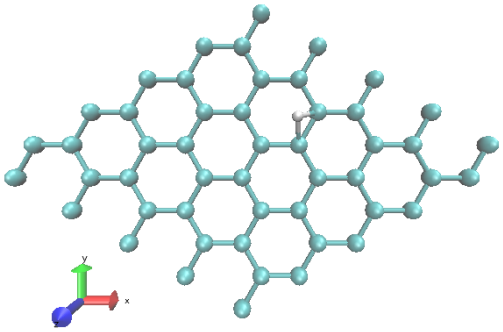

(b) The initial unit cell, with hydrogen atom in its preferred minimum energy position.

Figure 2.5: Determining the optimal position for an adsorbed hydrogen.

figure 2.6, and it should be noted that the activation energies for bond rotations in both directions have been reduced as a result of hydrogenation. When the chosen bond was rotated clockwise, the activation energy was reduced from 31 eV to 26.5 eV; and when the bond in question was rotated in the opposite direction, and the activation energy is reduced from 31 eV to 23 eV. Thus we have shown that the presence of adsorbed atomic hydrogen reduces the energy barrier for Stone-Wales defect formation. As an aside, we

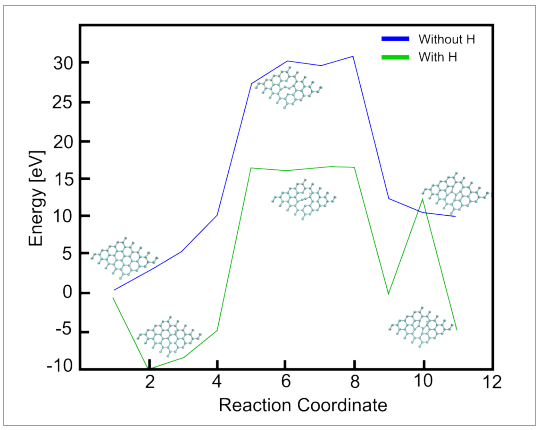

(a) Effect of hydrogen atom on the Stone-Wales defect formation by a clockwise bond rotation.

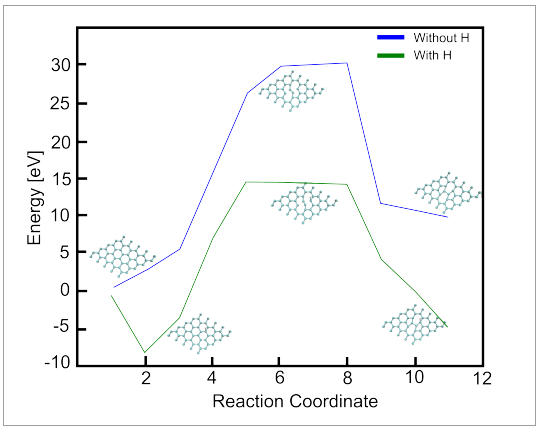

(b) Effect of hydrogen atom on the Stone-Wales defect formation by an anticlockwise bond rotation.

Figure 2.6: Effect of adsorbed hydrogen in Stone-Wales defect formation. In both cases, presence of hydrogen increased the probability of defect formation. For reaction pathways with hydrogen, we observe a drop in energy due to unit cell relaxation in response to hydrogen adsorption.

also observe that in the hydrogenated case, the reaction pathways show an initial drop in energy. This is because the hydrogen was adsorbed to (and energy minimized assuming) a planar graphene sheet. Once all atoms were allowed to move during the reaction pathway computation, the unit cells immediately relax in response. A separate geometry minimization is not necessary here as long as the genetic heuristic samples various atomic configurations, and this relaxation is accounted for as demonstrated in figures 2.6 and 2.7.

Another difference also observed in the reaction pathways, and presented in figure 2.7 is the directional preference for bond rotation, in the presence of adsorbed atomic hydrogen. Unlike the non-adsorbed case, the two directions of bond rotation are no longer chemically equivalent. As a result, one expects a higher probability of bond-rotation in the anticlockwise direction for a Stone-Wales defect formation.

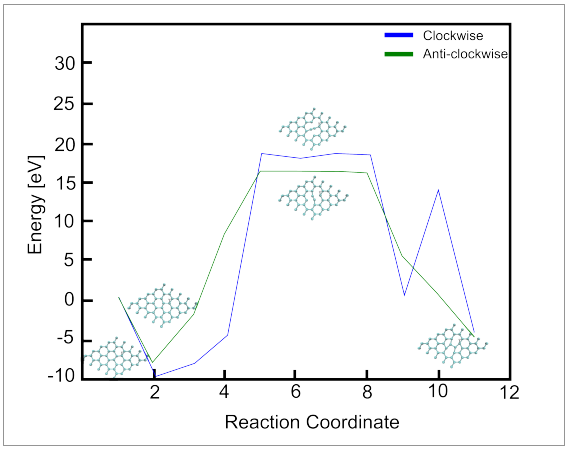

Figure 2.7: Comparison of energy barriers for Stone-Wales defect formation in the presence of a hydrogen atom. We can see that there is a directional preference to bond rotation

2.6 Application to an armchair nanotube

We apply the same set of computations now to a carbon nanotube. In this example, a (3,3) arm-chair nanotube is used with periodic boundary conditions along its axis direction. Identical computations are done to obtain the reaction pathways, in two cases - with and without an adsorbed atomic hydrogen. The best configuration for adsorbing atomic hydrogen is determined, again by sampling the (x,y,z) region around the nanotube while keeping the nanotube fixed, and choosing the minimum energy configuration. Unlike for planar graphene, an adsorption of an atomic hydrogen does not increase the probability of defect formation, as seen in figure 2.8.

One possible reason the results from the graphene unit cell do not transfer to this problem, is the high curvature of a small-index nanotube. It has been shown that the behavior of electrons is 1-dimensional in nanotubes and nanowires. Van Hove singularities, which are discontinuities in the density of states [59] have been measured for nanotubes. Going from graphene sheets to a (3,3) carbon-nanotube, the bonding between carbon atoms is still covalent sp^2, however, the electrons are no longer confined to a particular plane. We should also note that the bond rotations involved in Stone-Wales defect formation are not planar in these nanotubes. It is also worth considering that as we increase the nanotube indices (m,n) and therefore its radius, the curvature becomes less severe, and results from graphene may translate to nanotubes of larger diameter.

Furthermore, each type of nanotube has its own material properties, including metallic, semi-metallic and

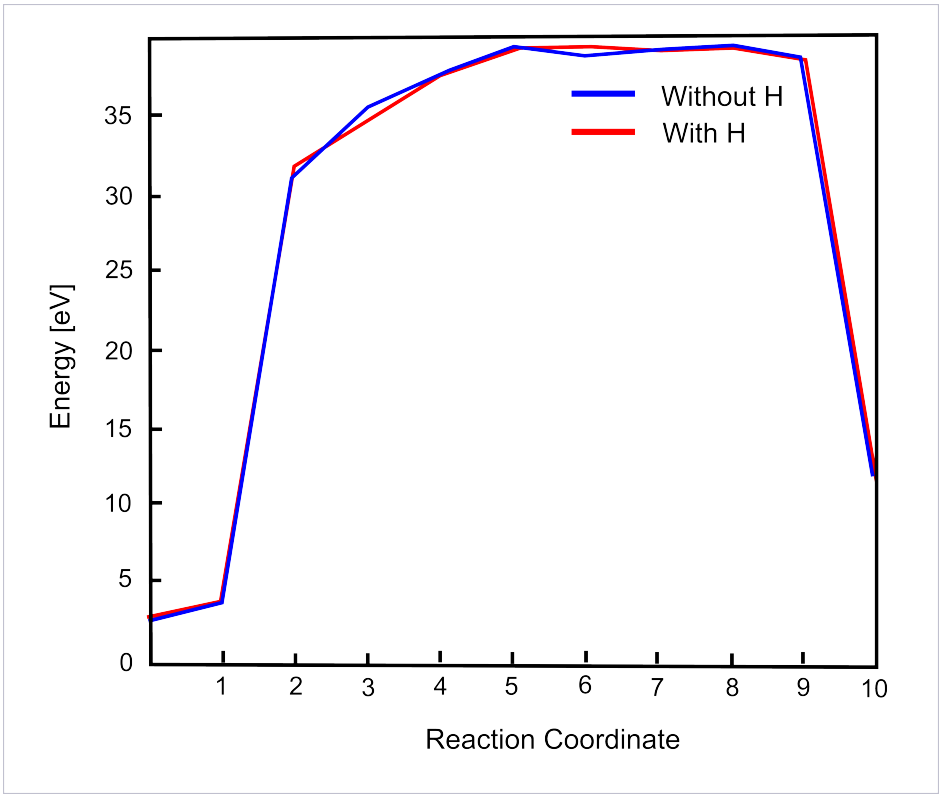

Figure 2.8: Defect formation with and without hydrogen. We see that adding hydrogen does not seem to change the reaction pathway or its activation energy.

insulating behavior, leading to interesting questions, such as whether the presence of a Stone-Wales defect attracts hydrogen adsorption, or whether presence of a hydrogen atom facilitates defect formation, and how their dynamics affect one another.

From the results of this chapter, we conclude that the presence of a hydrogen atom, here a stand-in for a generic functional group, weakens the planar $C - C$ bond, leading to easier formation of Stone-Wales defect. However, hydrogen adsorption had no discernible effect on Stone-Wales defect formation in one type of nanotube tested, for possible reasons listed above.

CHAPTER 3

OPTICAL ABSORPTION RATES

In this chapter, we investigate the optical properties of graphene and carbon nanotubes, and how different types of defects affect optical absorption. So far, the Hamiltonian used has been the time-independent tight-binding Hamiltonian, whose eigenvalues are the energy levels associated with the system.

$$\hat{H}\,|\psi\rangle = E\,|\psi\rangle \tag{3.1}$$

Within the single-electron approximation, an optical absorption occurs when an electron in a lower energy level is elevated to a higher energy level due to an incident electromagnetic field. So, an interaction Hamiltonian is necessary to include the effect of the incident external field.

$$\hat{H}_{tot} = \hat{H}_{TB} + \hat{H}_{INT} \tag{3.2}$$

Here, the interaction Hamiltonian H_{INT} is time-dependent because the electromagnetic field, presented as a classical field, is time-dependent. Furthermore, we can assume that the incident electromagnetic field is weaker in comparison to the atom-core potential, so that the time-dependent perturbation theory to first order is applicable [33]. The weak electromagnetic field varies harmonically with time $e^{-i\omega t}$, which simplifies this analysis further and gives rise to the well known Fermi's golden rule [8] [30]. Fermi's golden rule, described in section 3.3, determines the rates of transition between two energy levels, and will be used to approximate the rate of absorption of incident electromagnetic fields.

While the harmonic-time-variation of electromagnetic fields ($e^{-i\omega t}$), is fixed, the spatial dependence of the interaction Hamiltonian depends on the electromagnetic gauge used, and they are related by a unitary transformation. Generally, the interaction Hamiltonian terms are written either in the standard form[8]

$$H_{int} = \mathbf{p} \cdot \mathbf{A} \tag{3.3}$$

or in the dipole approximation [39]

$$H_{int} = \mathbf{d} \cdot \mathbf{E}(\mathbf{r}, \mathbf{t}) \tag{3.4}$$

where $\mathbf{p}$ represents the momentum, $\mathbf{A}(\mathbf{r}, \mathbf{t})$ is the electromagnetic vector potential, $\mathbf{d}(\mathbf{r})$ is the dipole moment,

and $\mathbf{E}(\mathbf{r}, \mathbf{t})$ is the electric field. The second form, the Goppert-Mayer approximation, gives the interaction Hamiltonian in terms of a gauge-independent quantity, the electric field. The dipole moment of a collection of charges can also be computed in a straightforward manner, even in the single electron approximation. As a result, the dipole approximation is widely used to compute the excitation of electrons due to the electromagnetic field. In this chapter, we follow the Goppert-Mayer treatment, which we extend to include the impact of higher multipoles. The interaction Hamiltonian used in this chapter is developed in [4] [48] [49] and is related to quantum electrodynamics in the non-relativistic $c \to \infty$ limit [9].

We begin by first looking at the Goppert-Mayer approximation to deduce simple but powerful conclusions about absorption of light by individual atoms.

3.1 Optical absorption by a single atom

Let us consider a hydrogenic atom, with its usual s-p-d-f orbitals, and with its unperturbed Hamiltonian of the form :

$$\hat{H}_{atom} = \begin{bmatrix} \epsilon_{1s} & 0 & 0 & 0 & 0 \\ 0 & \epsilon_{2s} & 0 & 0 & 0 \\ 0 & 0 & \epsilon_{px} & 0 & 0 \\ 0 & 0 & 0 & \epsilon_{py} & 0 \\ 0 & 0 & 0 & 0 & \epsilon_{pz} \end{bmatrix} \tag{3.5}$$

In the absence of an external perturbation (such as bonding or incident electromagnetic field), an electron in $|1s\rangle$ orbital, defined by its radial and angular wavefunctions will remain in that eigenstate forever, as the wavefunction oscillates with frequency given by $\hbar\omega = \epsilon_{1s}$. If we now introduce external light and wish to know the effect of this external field on the electron, the total Hamiltonian is given by:

$$H_{total} = H_{atom} + H_{field} + H_{interaction} \tag{3.6}$$

In the long wavelength approximation, the external field affects the material but not vice-versa, so the field Hamiltonian H_{field} is assumed a constant, and removed for now. Following Goppert-Mayer [39], we first assume that the interaction between the atomic electron density and electromagnetic field occurs through the dipole moment. The magnetic dipole-magnetic field interaction is smaller and is neglected. Then, the interaction between an atom and an electromagnetic field in the dipole-approximation is given by:

$$H_{interaction} = \mathbf{d} \cdot \mathbf{E} e^{-i\omega t} \tag{3.7}$$

where $\mathbf{d}$ is the dipole of the electronic charge distribution

$$\mathbf{d} = \langle\psi|\hat{r}|\psi\rangle = \int \psi^*(\mathbf{x})\hat{\mathbf{x}}\psi(\mathbf{x})d^3\mathbf{x} \tag{3.8}$$

$\mathbf{E}$ is the applied electric field and is not expected to change within the the atomic radius. The time-dependence, as usual, is due to the harmonic time dependence of the electromagnetic field.

For the purposes of calculation, let us assume that the direction of the electric field $\mathbf{E}$ is along the z-axis. Because the atom is spherically symmetric when it is not bonded to other systems, this simplification makes it easier to calculate the interaction Hamiltonian, and this is where the symmetry of the atoms determines whether an electron in a $|1s\rangle$ orbital can transition to the higher $|2s\rangle$ orbital; this particular transition cannot occur because the integral

$$\mathbf{d} = \int \psi^*_{1s}(\mathbf{x})\hat{\mathbf{x}}\psi_{2s}(\mathbf{x})d^3\mathbf{x} = \mathbf{0} \tag{3.9}$$

In this way, the symmetry of atomic orbitals gives a selection of possible transitions. The interaction Hamiltonian for a hydrogen-like atom including orbitals from $1s-$ to $2pz$ orbitals will look like :

$$H_{int} = \begin{bmatrix} 0 & 0 & \checkmark & \checkmark & \checkmark \\ 0 & 0 & \checkmark & \checkmark & \checkmark \\ \checkmark & \checkmark & 0 & 0 & 0 \\ \checkmark & \checkmark & 0 & 0 & 0 \\ \checkmark & \checkmark & 0 & 0 & 0 \end{bmatrix} \tag{3.10}$$

In tight-binding computations only valence electrons are considered, electrons from the core energy levels can be excited but they may require energies in order of 100 eVs, which is beyond our range of investigation by orders of magnitude. Therefore, 2s and 2p orbitals are considered and we can reduce the interaction Hamiltonian to

$$H^{atom}_{int} = \begin{bmatrix} 0 & \checkmark & \checkmark & \checkmark \\ \checkmark & 0 & 0 & 0 \\ \checkmark & 0 & 0 & 0 \\ \checkmark & 0 & 0 & 0 \end{bmatrix} \tag{3.11}$$

Although the dipole-approximation is a simplified representation, and we will be using the polarizability field with higher multipoles, the above selection rules give a general idea of the importance of the rotational symmetry of the atomic orbitals. When atoms form bonds, they are no longer rotationally symmetric as the electron distribution around an atom is re-arranged. The effects of bonding and the direction of the applied electric field, together influence the optical properties of bonded materials.

3.2 Hamiltonian of light-matter interaction

In section 3.1, we discussed the impact of rotational symmetry on selecting which electron transitions are possible in the dipole approximation. In this section, we now introduce the multipolar form of the perturbation Hamiltonian H' that will be used in later sections. In 1970, Woolley introduced the total Hamiltonian for studying the interaction of a hydrogen-like atom with electromagnetic fields [65]. The same total Hamiltonian can also be expressed in a multipolar form, after applying a gauge transformation (see Power Zineau [4], Claude-Cohen [9], Goppert-Mayer [39]). From equation 34 in [65]:

$$H = H^{ATOM} + H^{RADIATION} - e^{i\omega t} \int d\tau \mathbf{P}(\mathbf{r}) \cdot \mathbf{e}^{\perp}(\mathbf{r}) + \text{terms in } \mathbf{b}(\mathbf{r}) \cdot \mathbf{M}(\mathbf{r}) + \text{renormalization terms} \quad (3.12)$$

In our calculations, the Hamiltonian of the atomic system is quantum mechanical, and the radiation Hamiltonian is taken to be classical. $\mathbf{e}$ and $\mathbf{b}$ are the electric and magnetic fields respectively, and $\mathbf{e}^{\perp}$ is used to distinguish the transverse electromagnetic field from other externally applied electric fields (for example, a voltage difference applied across the unit cell or device). Lower case $\mathbf{e}$ and $\mathbf{b}$ are used instead of $\mathbf{E}$ and $\mathbf{B}$ to indicate that these are local microscopic electric and magnetic fields. Polarizability ($\mathbf{P}(\mathbf{r})$) and magnetization ($\mathbf{M}(\mathbf{r})$), both are the multipole expansions of electric dipole and magnetic moments, and act as source terms in Maxwell's equations. When the magnetic field dependence is ignored, and assuming that the electromagnetic field remains unchanged macroscopically, the following equation is obtained for the atom-field interacting system:

$$H = H^{ATOM} - e^{i\omega t} \int d\tau \mathbf{P}(\mathbf{r}) \cdot \mathbf{e}^{\perp}(\mathbf{r}) \quad (3.13)$$

where

$$H'(r) = -e^{i\omega t} \int d\tau \mathbf{P}(\mathbf{r}) \cdot \mathbf{e}^{\perp}(\mathbf{r}) \quad (3.14)$$

The matrix elements of this perturbation Hamiltonian, in the tight-binding basis, are given by:

$$\langle \phi_s^A | H' | \phi_{px}^A \rangle = -e^{i\omega t} \int d^3\mathbf{r} \mathbf{P}_{s,p}^{A,A}(\mathbf{r}) \cdot \mathbf{e}_{\perp} \quad (3.15)$$

where ϕ_s^A and ϕ_{px}^A represent the s and px orbitals on atom A. In the long wavelength approximation of the electromagnetic field, the electric field $\mathbf{e} = |\mathbf{E}| \exp[i(\mathbf{k} \cdot \mathbf{r} - \omega t)]$ is uniform in the neighborhood of the atom.As a result, the integral in the perturbation Hamiltonian can be simplified to

$$\langle \phi_s^A | H' | \phi_{px}^A \rangle = -e^{i\omega t} |\mathbf{E}| \left(\hat{\mathbf{n}} \cdot \int d^3\mathbf{r} \mathbf{P}_{s,px}^{A,A}(\mathbf{r}) \right) \quad (3.16)$$

We now are left to compute the value of the dot product between the polarizability vector of the electron

distribution, and the applied electric field. The polarizability $\mathbf{P}(\mathbf{r})$ is computed as follows

$$\mathbf{P}(\mathbf{r}) = -q \sum_{\alpha}^{electrons} \mathbf{r}_\alpha \int \delta(\mathbf{r} - \lambda \mathbf{r}_\alpha) d\lambda \tag{3.17a}$$

and can be written in terms of the single electron wavefunction as ,

$$\mathbf{P}(\mathbf{r}) = -q \int \psi^*(\mathbf{x}) \left[\int_0^1 \mathbf{x} \delta(\mathbf{r} - \lambda \mathbf{x}) d\lambda \right] \psi(\mathbf{x}) \mathbf{d^3 x} \tag{3.17b}$$

For ϕ_i and ϕ_j, two orbitals from the tight-binding basis set, the electron polarizability field $\mathbf{P}(\mathbf{r})$ is given by

$$\mathbf{P}_{ij}(\mathbf{r}) = -q \int d^3\mathbf{x} \int_0^1 \phi_i^*(\mathbf{x}) \mathbf{x} \delta(\mathbf{r} - \lambda \mathbf{x}) \phi_j(\mathbf{x}) d\lambda \tag{3.17c}$$

To compute values of the above integral, we use tight-binding orbitals of the form $\phi(r, \theta, \phi) = R_{nl}(r) Y_{lm}(\theta, \phi)$, where Y_{lm} is the spherical harmonic part of the orbital, and $R_{nl}(r)$ is the radial wavefunction of in the extended huckel orbital form [24]

$$R_{nl}(r) = K \cdot \frac{r^n}{\sqrt{2n!}} \left[C_1 e^{-\alpha r} + C_2 e^{-\beta r} \right] \tag{3.18}$$

We now go back to determining the elements of the perturbation Hamiltonian presented in equation 3.16. The elements of the perturbation Hamiltonian, H' are given by:

$$H'_{ij} = \langle \phi_i | H' | \phi_j \rangle = -e^{i\omega t} |\mathbf{E}| \int \mathrm{d}^3\mathbf{r} \left(\hat{\mathbf{n}} \cdot \mathbf{P}_{ij}(\mathbf{r}) \right) \tag{3.19}$$

In constructing the above Hamiltonian, we note that while bonding does not affect $\hat{\mathbf{n}}$ or the matrix elements of $\mathbf{P_{ij}}(\mathbf{r})$ directly, the optical absorption values are determined when this matrix is multiplied by eigenstates of the tight-binding Hamiltonian. For example, an eigenstate that represents sp^2 bonding will give different weights to the various components of $\mathbf{P_{ij}}(\mathbf{r})$ compared to an eigenstate that corresponds to sp^3bonding. We also note the effect of the direction of electric field polarization $\hat{\mathbf{n}}$ in determining the magnitude of corresponding elements. In the following sections, we present the rates of optical absorption by a graphene unit cell, and the effect of defects.

3.3 Rates of optical absorption

In the first and second chapters, we have set up computations for energy levels and bandstructure of materials. In the following analysis we assume that these energy levels will remain unaffected by the absorption or emission of photons. (Alternatives to this assumption exist, but they are computationally expensive methods influenced by many-body approximations, and are discussed briefly at the end of this chapter.)

In the single electron approximation, an electron may or may not occupy a given energy level, i.e. its occupation $f(E_i)$ given by the Fermi-Dirac distribution may change, but the tight-binding Hamiltonian itself does not. We can then use Fermi's golden rule for transition probabilities. Up to first order in perturbation theory, the rate of transition from a lower energy level E_q to a higher energy state at energy E_k, due to an electromagnetic field with $energy = \hbar\omega$ is given by [8]:

$$W_{abs} = |\langle k| H' |q\rangle|^2 \delta(E_k - E_q - \hbar\omega) \tag{3.20}$$

For a photon to be absorbed, the electronic states $|q\rangle$ and $|k\rangle$ must be occupied and empty respectively. At non-zero temperature, the probability of occupation and vacancy are given by $f(E_q)$ and $(1 - f(E_k))$ respectively . Including this observation, the rate at which a state at lower energy E_q transitions to a state at higher energy E_k is given by the equation

$$R_{q\to k} = \sum_{k,q} |\langle q| H' |k\rangle|^2 \delta(E_k - E_q - \hbar\omega) f_q(1 - f_k) \tag{3.21}$$

Similarly, the rate of the opposite transition is given by:

$$R_{q\leftarrow k} = \sum_{k,q} |\langle q| H' |k\rangle|^2 \delta(E_k - E_q - \hbar\omega) f_k(1 - f_q) \tag{3.22}$$

The combination of these two rates, gives the net rate of transition from E_q to E_k, or the absorption of a photon of energy $\hbar\omega$

$$R_{net} = R_{q\to k} - R_{q\leftarrow k} \tag{3.23}$$

$$= \sum_{k,q} |\langle q| H' |k\rangle|^2 \delta(E_k - E_q - \hbar\omega)(f_q - f_k) \tag{3.24}$$

Above, we have used the fact that the dirac-delta function is symmetric

$$\delta(E_k - E_q - \hbar\omega) = \delta(E_k - E_q - \hbar\omega) \tag{3.25}$$

3.4 Local contribution to optical absorption

In this section, we extend our discussion of the absorption rates discussed above. We note that the states $|k\rangle$ and $|q\rangle$ are the single electron wavefunctions in tight-binding. As such, they can be written as linear combinations of atomic orbitals, or be projected into specific atomic orbitals. By using the projection sum property,

$$\sum_r |r\rangle \langle r| = 1 \tag{3.26}$$

we can rewrite equation 3.24, as the sum of atomic contributions as follows

$$W_{absorption}(\omega) = \sum_{k,q} \langle q|H'|k\rangle \langle k|H'|q\rangle \, \delta(E_k - E_q - \hbar\omega)(f_q - f_k) \tag{3.27a}$$

$$= \sum_{k,q} \langle q|H' \left[\sum_r |r\rangle \langle r|\right] k\rangle \langle k|H'|q\rangle \, \delta(E_k - E_q - \hbar\omega)(f_q - f_k) \tag{3.27b}$$

$$= \sum_r \left[\sum_{k,q} \langle q|H'|r\rangle \langle r|k\rangle \langle k|H'|q\rangle \, \delta(E_k - E_q - \hbar\omega)(f_q - f_k)\right] \tag{3.27c}$$

$$= \sum_r W_{abs}(\omega, |r\rangle) \tag{3.27d}$$

3.5 Application to graphene sheets

3.5.1 Setup of graphene sheet and defect structures considered

The above calculations are used to study the $\Gamma-$point optical absorption in graphene. We apply the above formulation to a unit cell containing 50 carbon atoms with periodic boundary conditions, and investigate the effect of defects on the total and local absorption properties.

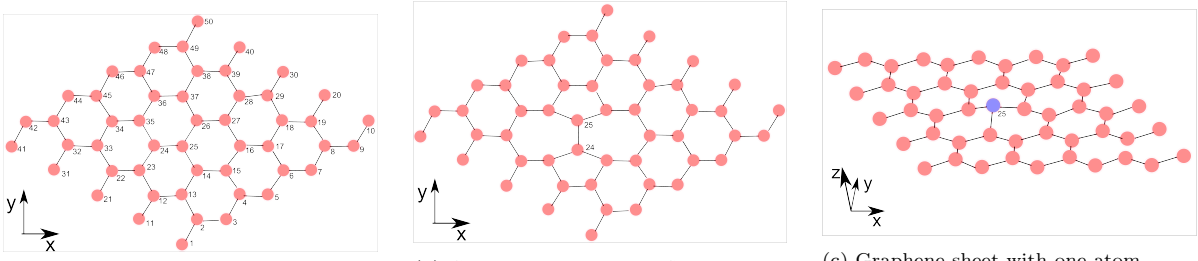

(a) Perfect planar graphene sheet.

(b) Graphene sheet with a Stone-Wales defect.

(c) Graphene sheet with one atom displaced out of plane.

Figure 3.1: Set up of various graphene-based structures; their total and local optical absorption properties will be investigated.

As represented in figure 3.1, three unit cells are considered: (a) a perfect graphene unit cell, (b) a Stone-Wales defect, and (c) a perfect graphene unit cell but with one atom raised above the plane. The tight-binding Hamiltonian is constructed via the same set of parameters used in chapter 2, and the absorption rates at the $\Gamma-$ point are computed using equations 3.24 and 3.27. For this computation, the incident electromagnetic field is linearly polarized such that the electric field is oriented along the z-axis, perpendicular to the graphene sheet.

3.5.2 Results I : Total absorption rates

The calculated total absorption rates of the three unit cells are shown in figure 3.2 (a), (b) and (c) respectively. A perfect graphene unit cell only absorbs electromagnetic energy at 12.8 eV, whereas the addition of a Stone-Wales defect broadens the range of frequencies absorbed, and increases the rate of absorption. On the other hand, an out-of-plane displacement of one carbon atom results in a broader range of frequencies being absorbed, which is accompanied by a decrease in the magnitude of absorption rates. The addition of a defect introduces more energy levels in comparison to the perfect case, so more transitions chosen by $\delta(E_k - E_q - \hbar\omega)$ become possible. Furthermore, defects also change the hybridization of bonds (sp^2-bonds in the perfect case are disturbed by defects), and thus affect the direction and magnitude of the polarizability vector $\mathbf{P}(\mathbf{r})$; this then changes the relative magnitudes of the various inter-orbital selections.

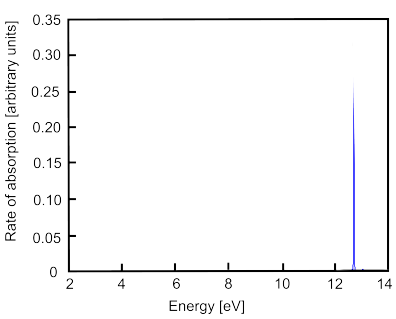

(a) Optical absorption observed at around 12 eV.

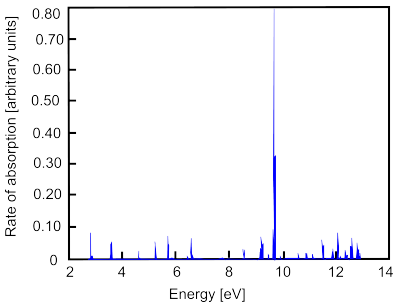

(b) The Stone-Wales defect causes wider range of frequencies to be absorbed, at increased rates of absorption.

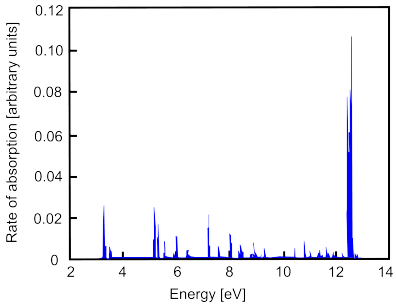

(c) Out-of-plane displacement of an atom results in a wider range of frequencies absorbed, but with reduced rates.

Figure 3.2: The effect of defects on total absorption properties. Three unit cells are considered (a) a perfect graphene unit cell, (b) unit cell with a Stone-Wales defect and (c) unit cell with one carbon atom displaced out of plane. The presence of defects broadens the absorption spectra, but may increase or decrease the absolute rate of absorption.

3.5.3 Results II : Atomic contribution to total absorption

Next, the atomic contributions within each unit cell, for the first observed absorption peak, are investigated using equation 3.27 and presented in figure 3.3. We observe that while all atoms contribute almost equally to the absorption peak for the perfect graphene unit cell, for the Stone-Wales defect case, atoms near and around the Stone-Wales defect are responsible for the absorption peak at 2.8eV. Similarly, when one atom is displaced out of plane, the displaced atom has the dominant contribution to the lower energy absorption at around 3eV, as seen in figure 3.3(c).

In this section, we showed the calculation of optical absorption rates in the context of tight-binding, and then presented how the impact of defects on optical absorption can be attributed to atoms. In the next section, we will extend these calculations to include nanotubes and their defect structures. We will also show the relationship between the rates of optical absorption and the dielectric function.

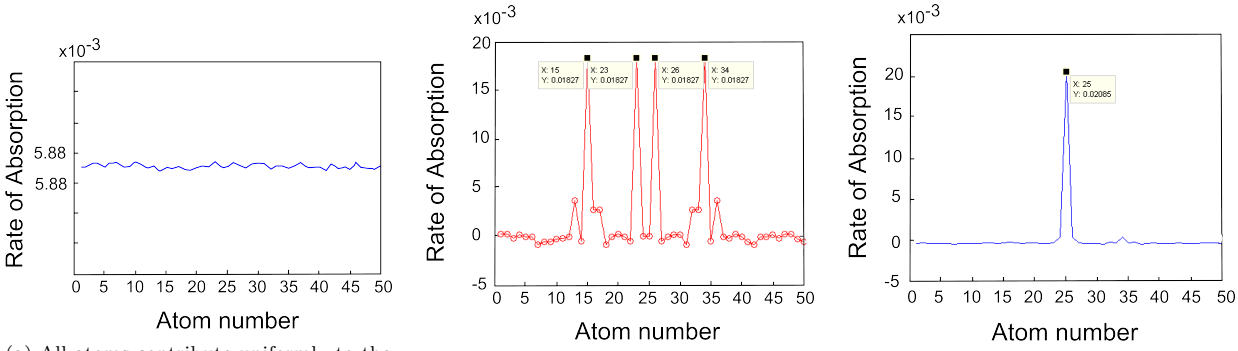

(a) All atoms contribute uniformly to the total absorption.

(b) Atoms closest to the defect contribute most to absorption of the first resonant frequency.

(c) The atom displaced out of plane contributes most to the first absorption peak.

Figure 3.3: Atomic contributions to the total absorption at the first resonant energies observed in figure 3.2. (a) perfect graphene cell, whose first resonance is observed at $\hbar\omega = 12.8$ eV. (b) unit cell with a Stone-Wales defect, where the first resonance is observed at $\hbar\omega = 2.89$ eV, and (c) unit cell with an atom displaced out of plane, where the first resonance observed is at 3eV.

3.6 Application to carbon nanotubes

3.6.1 Setup of carbon nanotubes considered

We now consider optical absorption in nanotubes, which are 1-dimensional structures constructed by "rolling-up" graphene sheets at various geometries; three types of carbon nanotubes are chosen - (a) an armchair terminated (3,3),(b) a zigzag terminated (5,0), and (c) a chiral (4,2) nanotube, all of which are presented in figure 3.4. Periodic boundary conditions are applied along the nanotube axis, and as in the previous section, computations are made at the $\Gamma-$ point. The incident electric field is polarized either perpendicular to, or along the nanotube-axis, and matches the conditions in the time-dependent LDA computations in [37]. The long-wavelength approximation $\lambda >> a$ still holds as the wavelengths of the electromagnetic fields considered, are in hundreds of nanometers.

The electronic properties of carbon nanotubes depend on the pair of indices (m,n), and a periodic table exists to classify all possible types of nanotubes constructed. The radius of the nanotube is determined by the (m,n) indices, and the lattice parameters $\mathbf{a_1} = 2.46\left[\frac{\sqrt{3}}{2} \quad \frac{1}{2} \quad 0\right]$, and $\mathbf{a_2} = 2.46\left[\frac{\sqrt{3}}{2} \quad -\frac{1}{2} \quad 0\right]$. To ensure that the nanotubes are not strained, the total energy is minimized with respect to the lattice constant, and the chemical potential is calculated by using electron number conservation, such that

$$\sum_i \frac{1}{1+\exp\left[\frac{E_i-\mu}{k_B T}\right]} = N_{electrons} \tag{3.28}$$

A built-in minimizer in MATLAB that accepts an initial guess and tries to find an interval where $LHS-RHS$ changes signs, is used to calculate μ. The temperature in the Fermi-Dirac distribution is set to 300 K, and

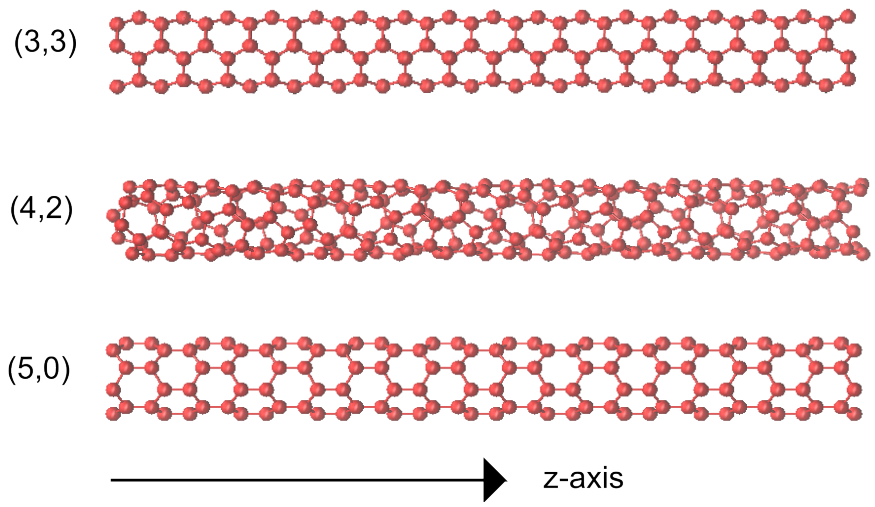

Figure 3.4: The absorption spectrum is computed for three different types of carbon nanotubes : metallic, non-metallic and insulating, as shown from top to bottom respectively. Defects are then added to these nanotubes later.

the $\delta(E_i - E_j - \hbar\omega)$ function that determines the possibility of resonance is approximated by a Gaussian, or

$$\delta(x) \approx \frac{1}{\sqrt{2\pi\sigma^2}} \exp\left[-\frac{x^2}{2\sigma^2}\right] \tag{3.29}$$

where $\sigma = 0.01$.

3.6.2 Defining the dielectric constant in terms of optical absorption rates

For purposes of comparison with values in literature, the imaginary part of the dielectric function is computed as a measure of optical absorption. The rate of absorption is related to the dielectric function - in particular to the imaginary part of the permittivity $\epsilon(\omega) = \epsilon_1(\omega) + i\epsilon_2(\omega)$, where $\epsilon_2(\omega)$ is given by

$$\epsilon_2(w) = \frac{\pi e^2}{{m_0}^2\omega^2} \cdot \frac{2}{V} R_{netConductionBulk}(\omega) \tag{3.30}$$

Here $\frac{2}{V}$ takes into account the fact that the quantity has been volume averaged. Furthermore, ϵ_1 can be calculated via the Kramers-Kronig relation:

$$Re(\epsilon(r,\omega)) = -\frac{1}{\omega}\int d\omega' \frac{Im(\epsilon(\omega'))}{(\omega - \omega')} \tag{3.31}$$

or

$$\epsilon_1(r,\omega) = -\frac{1}{\omega}\int d\omega' \frac{\epsilon_2(r,\omega')}{(\omega - \omega')} \tag{3.32}$$

So that we can get the dielectric function

$$\epsilon_{complex}(r,\omega) = \epsilon_1(r,\omega) + i\epsilon_2(r,\omega) \tag{3.33}$$

In equation 3.27, we projected out the contribution of each atom to the total absorption by adding projection operators $\sum_r |r\rangle \langle r| = 1$. We manipulate the equation for dielectric constant in a similar way to obtain local, atomically projected contributions. Let us define a local $\epsilon_2(r, \omega)$ using the local absorption formula from equation 3.27, or

$$\epsilon_2(r, w) = \frac{\pi e^2}{{m_0}^2 \omega^2} W_{netConduction}(r, \omega) \tag{3.34a}$$

$$\epsilon_2(r, w) = \frac{\pi e^2}{{m_0}^2 \omega^2} \sum_{k,q} \langle q|H'|r\rangle \langle r|k\rangle \langle k|H'|q\rangle \delta(E_k - E_q - \hbar\omega)(f_q - f_k) \tag{3.34b}$$

This projection now allows us to write the total $\epsilon_2(\omega)$ as a sum of atomic orbital contributions, or

$$\epsilon_2(\omega) = \sum_{r \in \text{orbital basis}} \epsilon_2(r, \omega) \tag{3.34c}$$

3.6.3 Results I : Optical absorption properties of perfect nanotubes

The rates of optical absorption in (5,0), (4,2) and (3,3) carbon nanotubes when the electric field is along the x-axis, transverse to the nanotube axis, are shown in shown in figure 3.5. Compared to time-dependent Density Functional Theory (TDDFT) calculations for these nanotubes [37] where the computed absorption peaks were at 1.5 eV, 2.0 eV and 3.0 eV respectively, we have qualitative agreement despite using tight-binding parameters optimized for structure-prediction of hydrocarbons, and with non-self-consistent, orthogonal tight-binding.

When the incident light is polarized along the periodic axis of the nanotubes, we observe that the (3,3) carbon nanotube is transparent for frequencies under 5 eV, which is also consistent with experiment[32] and TDDFT calculation[37]. The results for (3,3) and the other two nanotubes are presented in figure 3.6.

3.6.4 Results II : Optical absorption properties of carbon nanotubes with defects

Finally, we investigate how defects change optical absorption in several different nanotubes. Three types of defects are considered for this purpose, and presented in figure 3.7 : (a) the Stone-Wales defect, (b) a line defect along the axis of the nanotube, and (c) a line defect along the circumference of the nanotube.

The rates of total optical absorption, and their variations due to nanotube index, defect type and the direction of linearly polarized light, are shown in figure 3.8. We note that the presence of a defect, almost always broadens the absorption spectrum to include a larger range of frequencies, instead of sharp peaks at particular resonant frequencies. Our model predicts the greatest shift in the absorption behavior of (3,3) nanotubes, where lower frequencies are absorbed in the presence of defects. In the case of (5,0) nanotubes,

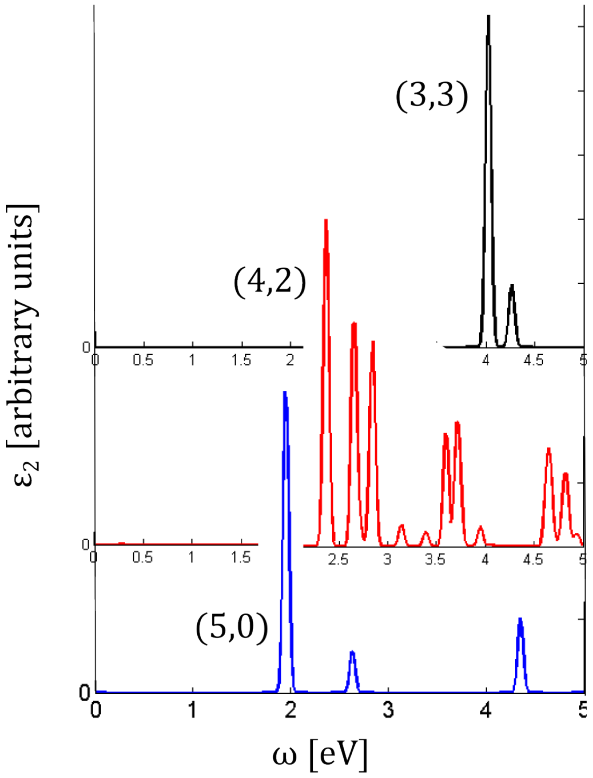

Figure 3.5: The absorption spectrum of the three perfect types of nanotubes with electric field polarization along the x-axis. The absorption spectra show qualitative agreement with the absorption spectra in [37], where the peaks were observed at 1.5 eV, 2.0 eV and 3.0 eV.

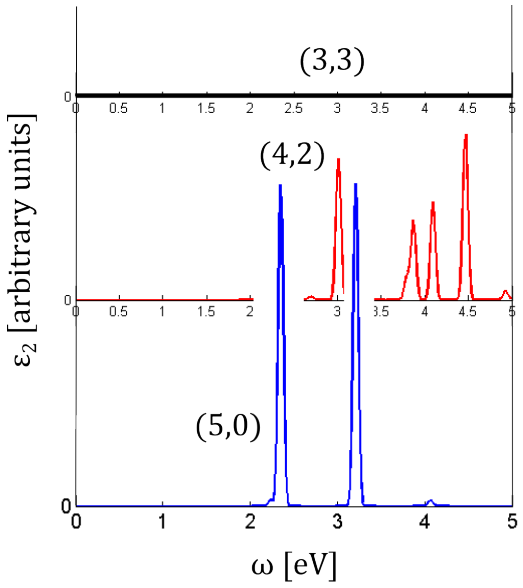

Figure 3.6: The absorption spectrum of the three perfect types of nanotubes with electric polarization along the z-axis. As predicted from experiments[32] and ab-initio[37] computations, there is no absorption observed for (3,3) nanotubes in this energy range, when the electric polarization is along the z-axis.

the presence of defects broadens the absorption spectrum, but significantly reduces the strength of the absorption. A similar effect of defects is seen in the (4,2) nanotubes, although the reduction in absorption

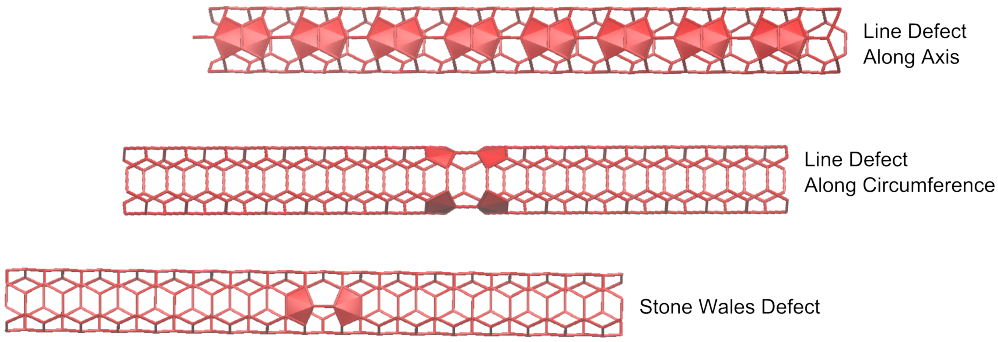

Figure 3.7: The three different types of defects considered in this manuscript, here demonstrated using a $(3,3)$ nanotube. Variations in the type of defect, and the type of nanotube (i.e. in the (m,n) indices), and the polarization of incident light affect absorption behavior.

probabilities are not as significant. On the other hand, in the presence of defects, not only does a (3,3) nanotube have absorption at a wider range of frequencies, it is also accompanied by increased rates of absorption at the previously resonant frequencies.

In conclusion, we note that while these results are dependent on the tight-binding parameterization and can be improved if self-consistent charge calculations are added, figure 3.8 presents the wide range of variations in nanotube type, electric field polarization and defects that can affect optical absorption, and that can be computed inexpensively within the tight-binding framework. The novelty of this approach is that we have introduced the polarizability field of an electronic state as the quantity that determines optical absorption, and presented an efficient way to compute this quantity. This, together with the ability to assign specific absorption contributions to particular orbitals or atoms, can be useful tools to accurately characterize optical properties of heterogeneous materials.

3.7 Alternative methods that incorporate many particle effects:

Other methods of computing the optical absorption of materials exist, and the results of Time-dependent Density Functional Theory (TDDFT) computation [37] which includes the impact of a time-dependent potential, were compared to our significantly inexpensive computations. In TDDFT, a functional form for the exchange correlation potential is chosen, and this often involves skill and experience in guessing the right form of the potential (for example, Local Density Approximation(LDA), Generalized Gradient Approximation (GGA)), or the right linear combination of potentials, so that the energy differences observed in experiments can be replicated. To my understanding, other post-DFT methods such as GW [23] and Bethe-Salpeter equation [50] deal with improving the accuracy of the single electron calculation by including many-body effects. Electrons interact with each other through the electromagnetic field, and the single particle picture (and with it the exchange correlation potential) emerges due to the nature of electromagnetic field, screening and statistics of electrons involved. Given the single electron picture, the GW method takes a Green's

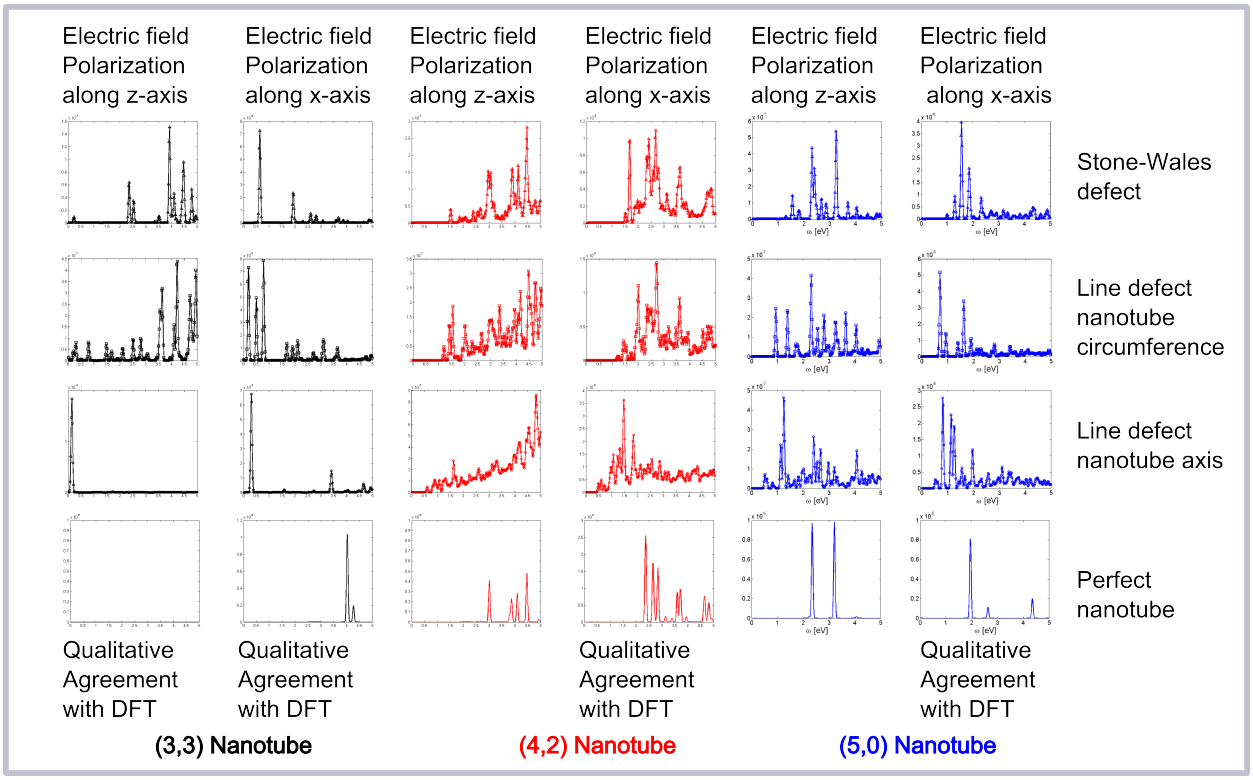

Figure 3.8: Variation of the total absorption spectra, and its dependence on the type of nanotube, direction of incident electric field, and type of defect.

function approach to compute the self-energy of the single electron quasiparticle. On the other hand, the Bethe-Salpeter equation approximates the many particle effects by introducing a hole quasi-particle. The interaction between the excited electron and the hole quasi-particle is then included to correct the excited state energy. As a result, the excited state can be at a lower energy level than previously anticipated from the uncorrected Hamiltonian.

CHAPTER 4

METHODS TO HANDLE LARGER SYSTEMS

In this chapter, we extend methods described in previous sections for use in larger systems where tight-binding becomes really powerful. Simulations for large systems usually run into an expensive computation - diagonalizing the Hamiltonian to determine system properties. Specifically, for a system of N atoms, the time taken for nearest neighbor calculation scales like $c \cdot N^2$, while the time for a brute-force eigenvalue calculation scales like N^3. These calculations become prohibitively expensive as the system size increases.

First, the problem of constructing the nearest neighors list is presented in section 4.1. By using a recursive map to store and search for atomic coordinates, the time taken to calculate nearest neighbors scales as $Nlog(N)$. These recursive trees are well-documented, and are called kd-trees [51]. We then introduce a toy problem to test large-systems-agorithms in section 4.3, and develop a way to avoid diagonalizing the Hamiltonian. There, we demonstrate how observables can be approximated by the Kernel Polynomial method, which scales as $O(N)$. This scaling of the Kernel Polynomial Method is well documented [54] [64]. Finally, in section 4.5, we present extensions to the Kernel Polynomial Method that allow us to evaluate quantities such as the total optical absorption rate, and its local atomic contributions, while still avoiding diagonalization.

4.1 Finding nearest neighbors

In order to construct the nearest neighbor list, a map containing all atomic coordinates is created. This map, as more atomic coordinates are added, is divided into octants, all of which are further recursively divided into smaller and smaller octants. Once the map is complete, it is possible to find the nearest atom, or the n-nearest atoms from a given point in space. Such a map of spatial points is called an octree, and is a well-established datastructure used in computer graphics and materials simulations [41]. As a result, several implementations for various purposes (parallel, serialized) in different languages can be found on the internet, or github . Here, we implement our own MATLAB implementation to be compatible with tight-binding code written for smaller systems, and presented in chapters 1-3. The general scheme is illustrated in figures 4.1 and 4.2, and below we describe a 2-dimensional lattice system with quadrants. This structure is called the quad-tree, since the two-dimensional space is divided into quadrants.

1. Set the origin of the system: $B0 = [0, 0]$, The index string for all atoms now begins with B.

2. Separate atoms that are not $B0$ into 5 parts: one group of atoms is within chosen r_{cutoff} of origin $B0$. These atoms are now indexed by Bx, and needs no more processing. The remaining atoms are divided into 4 groups depending on which quadrant they belong to with respect to $B0$. These four groups will be indexed as Ba, Bb, Bc and Bd .

3. For every group of atoms ending with a through d, a new origin, the average position of the atoms in that group is computed. Now that we have the new origins, atoms in each group are further separated into five groups, with $\{x, a, b, c, d\}$ added to the group name/index.

4. In computer science terms, the groups ending with x, which require no further division are called leaves. Iterate (3) until all the atoms belong to a leaf; this ensures that all nearest atoms within r_{cutoff} or in multiples of r_{cutoff} within a given point (x,y,z) can be reached in Nlog(N) time systematically.

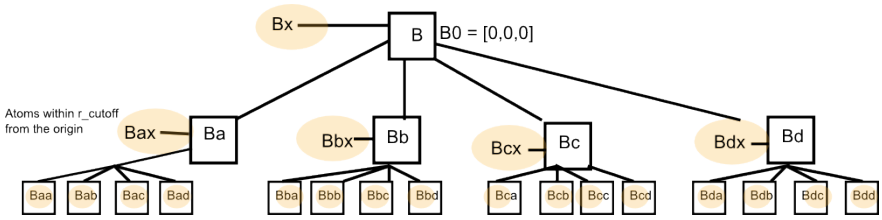

Figure 4.1: Schematic of the map as it starts organizing atoms in the input lattice into consecutively smaller quadrants.

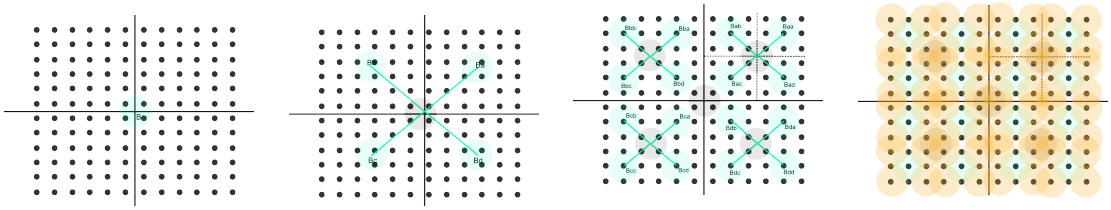

(a) Initial map - only the nearest neighbors close to origin are included.

(b) After first step - lattice is now divided into four quadrants.

(c) The map starts including more atoms, and more atoms are now within cutoff spheres.

(d) The map covers all atoms, and some spheres will overlap as they share neighboring atoms

Figure 4.2: Description of a recursive map to store atomic coordinates in two dimensions.

4.1.1 Performance comparison

The performance of the scheme described above is compared to the time taken by a direct for-loop computation, the results of which are presented in figure 4.3. Compared to the straightforward distance computation and sorting with for-loops, the octree structure has an initial cost associated with setting up the map, reflected in the longer runtime for the smallest, 1458-atom, unit cell. However, this initial overhead is soon offset by the performance improvement due to N(log(N)) scaling. We also note that for system sizes of around 60,000 atoms, the time taken by the for-loop implementation is greater than the time taken by

the octree by orders of magnitude. Furthermore, the scaling becomes more problematic as the system size approaches one million atoms.

Therefore, for simulations of systems with more than hundreds of thousands of atoms, the octree structure provides a huge performance boost in constructing nearest neighbor lists. Having established the method for creating neighbor lists, we can now apply these methods for unit cells of around 60,000 atoms, highlighted in figure 4.3.

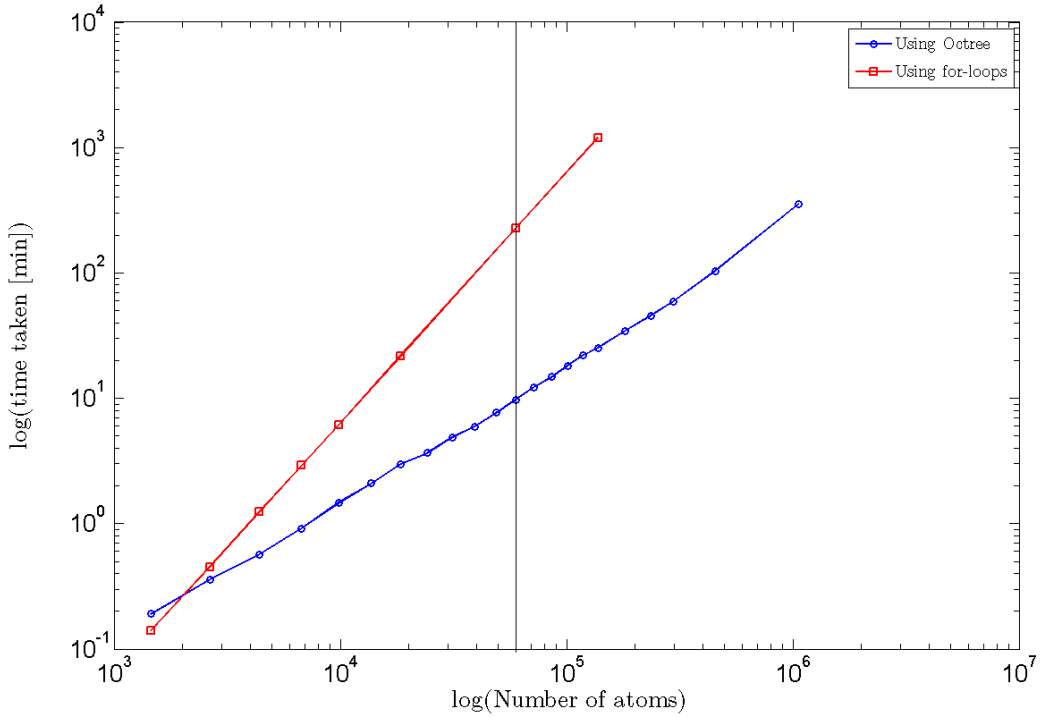

Figure 4.3: Times taken to obtain nearest neighbor list using the octree recursive map, compared to the time taken using for-loops. The vertical line crossing both graphs points to the times taken for a specific unit cell of 60,000 atoms; it takes (9 minutes vs 225 minutes) to construct the nearest neighbor list respectively.

4.2 Obtaining physical observables from the Hamiltonian

In this part of the methods section, the focus is on the next challenge - calculating physical quantities that depend on the eigenvalues of the system, without explicit diagonalization of large matrices. This is important because the scaling of direct diagonalization ($O(N^3)$) is worse than the scaling behavior for constructing nearest neighbor lists.

With the neighbor list provided by the octree implementation, the Hamiltonian can be built as described in chapters 1,2, and 3, using corresponding tight-binding parameters for different types of atoms and bonds. It is the next step, diagonalization, that becomes prohibitively expensive as the number of atoms grows.

Ideally, a method that scales linearly with system size is preferred.

Often, instead of the eigenvalues themselves, we are interested in some function of the eigenvalues, as in the case of the density of states:

$$dos(E) = \frac{1}{D}\sum_i \delta(E - E_i) \tag{4.1}$$

Or the local density of states:

$$ldos(A, E) = \frac{1}{D}\sum_{\phi_A}\sum_i \delta(E - E_i)|\langle\phi_A|\psi_i\rangle|^2 \tag{4.2}$$

where A is the atom whose contribution to the density of states we want to determine, $|\psi_i\rangle$ and E_i are the i-th eigenstate and eigenvalue of the Hamiltonian, respectively, and ϕ_A are the atomic orbitals of atom A. Moreover, observables can be written as a function of energy and the density of states. The observable $\hat{O}$ is often calculated in the form:

$$\langle O\rangle = \int O(E)f(E)dos(E)dE \tag{4.3}$$

where f(E) is the Fermi-Dirac distribution. In this context, the density of states and the local density of states will be the two quantities computed in this chapter. The Kernel Polynomial Method is one specific instance of polynomial expansion methods, that can be used in computing the *dos* and *ldos* in equations 4.1 and 4.2.

4.2.1 Kernel Polynomial Method I : general description of the moments method

In this subsection, we include a brief description of the moments method. In short, the moments method involves expanding the quantities of interest, in our case observables such as the total energy or the local density of states, in a series of orthogonal modes. These modes are often taken to be sines and cosines, but they can also be other polynomials.

Given two functions $f(x)$ and $g(x)$ defined on x such that $x \in [a, b] \subset \mathbb{R}$, and a weight w(x) that either depends on the type of coordinates used, or on the measure of integration d^3x involved, the inner product of functions $f(x)$ and $g(x)$, $\langle f|g\rangle$, is defined as:

$$\langle f|g\rangle = \int_a^b w(x)f^*(x)g(x)dx \tag{4.4}$$

A set of polynomials, $p_n(x) \in \mathbb{S}$, is said to be orthogonal with respect to $w(x)$ if their inner products

$$\langle p_m|p_n\rangle = \int_a^b w(x)p_m^*(x)p_n(x)dx = \delta_{m,n} \tag{4.5}$$

This orthogonality condition provides a way to expand any general function as a linear combination of

these orthgonal $p_n(x)$, given by

$$f(x) = \sum_n \alpha_n p_n(x) \tag{4.6}$$

with a straightforward way to obtain the coefficients α_n, or

$$\langle p_m | f(x) \rangle = \sum_n \alpha_n \langle p_m(x) | p_n(x) \rangle = \sum_n \alpha_n \delta_{m,n} \tag{4.7}$$

$$\langle p_m | f(x) \rangle = \alpha_m \tag{4.8}$$

4.2.2 Kernel Polynomial Method II: application using Chebyshev polynomials

Chebyshev polynomials are two related sets of orthogonal polynomials, widely used in approximation theory, and whose average errors and standard deviations have been quantified. (See Silver and Roder, [53] or Weisse [63] for more information and detailed review).

Both kinds of Chebyshev polynomials are defined over the interval $x : a \leq x \leq b$ where $[a, b] = [-1, 1]$, and the type of weight function

$$w(x) = \frac{1}{\pi \sqrt{1 - x^2}} \tag{4.9a}$$

$$w(x) = \pi \sqrt{1 - x^2} \tag{4.9b}$$

determines whether the polynomials are Chebyshev polynomials of the first kind $T_n(x)$, or of the second kind $U_n(x)$, respectively. In the following calculations, Chebyshev polynomials of the first kind are used, and some of their useful properties are as follows:

$$T_n(x) = \cos(n \ \cos^{-1}(x)) \tag{4.10a}$$

$$T_0(x) = 1 \tag{4.10b}$$

$$T_{-1}(x) = T_1(x) = x \tag{4.10c}$$

$$T_{m+1}(x) = 2xT_m(x) - T_{m-1}(x) \tag{4.10d}$$

In our calculation, the variable x is selected so that $\theta = \cos^{-1}(x)$ is uniformly distributed. Using these polynomials to expand the density of states expressions in equations 4.1 and 4.2, it is first necessary to scale the Hamiltonian H so that all eigenvalues fall within $[-1, 1]$:

$$\hat{H} = \frac{(H - b)}{a} \tag{4.11a}$$

$$\hat{E} = \frac{(E - b)}{a} \tag{4.11b}$$

where

$$a = \frac{E_{max} - E_{min}}{2 - \epsilon} \tag{4.11c}$$

$$b = \frac{E_{max} + E_{min}}{2} \tag{4.11d}$$

The maximum and minimum eigenvalues E_{max} and E_{min} can be found more easily with built in packages for sparse matrices. Restating equation 4.1:

$$dos(E) = \frac{1}{D} \sum_i \delta(E - E_i) \tag{4.12a}$$

for which D, the size of the Hamiltonian, will be ignored in the approximations following, and the energies(E) and eigenvalues(E_i) will be replaced by their scaled replacements x and x_i. The density of states can then be approximated by:

$$dos(x) = \sum_n \alpha_n T_n(x) \tag{4.12b}$$

Using the orthogonality of Chebyshev polynomials, we write:

$$\alpha_m = \int T_n(x) dos(x) w(x) dx \tag{4.12c}$$

Recalling that

$$\frac{1}{\pi\sqrt{1 - x^2}} = w(x)$$

for the first type of Chebyshev polynomial, $T_n(x)$. The computation of moments is then reformulated as a trace-of-matrix computation as follows:

$$\alpha_m = \int T_n(x) \sum_i \delta(x - x_i) w(x) \tag{4.12d}$$

Let $\alpha_m = \mu_m \; w(x)$ Then:

$$dos(x) = \frac{1}{D} \sum_n \frac{\mu_n T_n(x)}{\pi\sqrt{1 - x^2}} \tag{4.12e}$$

where the moments

$$\mu_n = \int T_n(x) \sum_i \delta(x - E_i) dx = \sum_i T_n(E_i) = Tr\left[T_n(\tilde{H})\right] \tag{4.12f}$$

The computation of a trace involves random vectors and matrix-vector multiplication, and the magnitude of the error of approximation depends on the number of random vectors used together with the distribution from which they are drawn. Despite this complication, an enormous speedup is obtained because the same set of random vectors can be used to compute the traces for all moments. Furthermore, the matrix-vector multiplication and trace calculation can easily be parallelized.

Next, we consider resolving the density of states to the atomic level. For large systems, the computation

of the local or projected density of states is even simpler and does not require trace computations, especially if the tight-binding basis is orthogonal. The local density of states is, restating equation 4.2:

$$ldos(A,E) = \frac{1}{D}\sum_{\phi_A}\sum_{i}\delta(E-E_i)|\langle\phi_A|\psi_i\rangle|^2 \tag{4.13a}$$

Rescaling the Hamiltonian as before, and expanding the local density of states in the same way,

$$ldos(A,x) \approx \sum_{n}\alpha_n T_n(x) \tag{4.13b}$$

we then compute the relevant moments $\alpha_n = \mu_n\ w(x)$ where we ignore the constant factor $\frac{1}{D}$ for now, and

$$\mu_n = \int T_n(x) ldos(A,x)dx = \int T_n(x)\sum_{\phi_A}\sum_{i}\delta(x-x_i)\langle\phi_A|\psi_i\rangle\langle\psi_i|\phi_A\rangle \tag{4.13c}$$

$$= \sum_{\phi_A}\sum_{i}\langle\phi_A|T_n(\tilde{H})|\psi_i\rangle\langle\psi_i|\phi_A\rangle \tag{4.13d}$$

$$= \sum_{\phi_A}\langle\phi_A|T_n(\tilde{H})|\sum_{i}\psi_i\rangle\langle\psi_i|\phi_A\rangle \tag{4.13e}$$

Using the orthogonality of eigenvectors in non-degenerate Hamiltonians, we can write $\sum_i |\psi_i\rangle\langle\psi_i| = 1$, which reduces the moment computation to a simple scalar evaluation of:

$$\mu_n = \sum_{\phi_A}\langle\phi_A|T_n(\tilde{H})|\phi_A\rangle \tag{4.13f}$$

Therefore, the local density of states, on a particular atom A at the rescaled energy x is given by:

$$ldos(x,A) = \frac{1}{D}\sum_{n}\frac{\mu_n T_n(x)}{\pi\sqrt{1-x^2}} \tag{4.13g}$$

The only difference in the local density of states computation, compared to the total density of states, is the simpler way in which the moments can be calculated.

4.3 Application

4.3.1 InAs quantum dots in GaAs matrix

In this section, we apply the methods discussed in sections 4.1 and 4.2 for a large representative system, such as an InAs quantum dot in a GaAs matrix. GaAs and InAs are both III-V semiconductors with zinc-blende crystal structures [3], but their bandgaps are 1.424 eV, and 0.354 eV respectively. The bandstructures of both pure crystals may be calculated using tight-binding parameters, and are presented in figure 4.4. As a

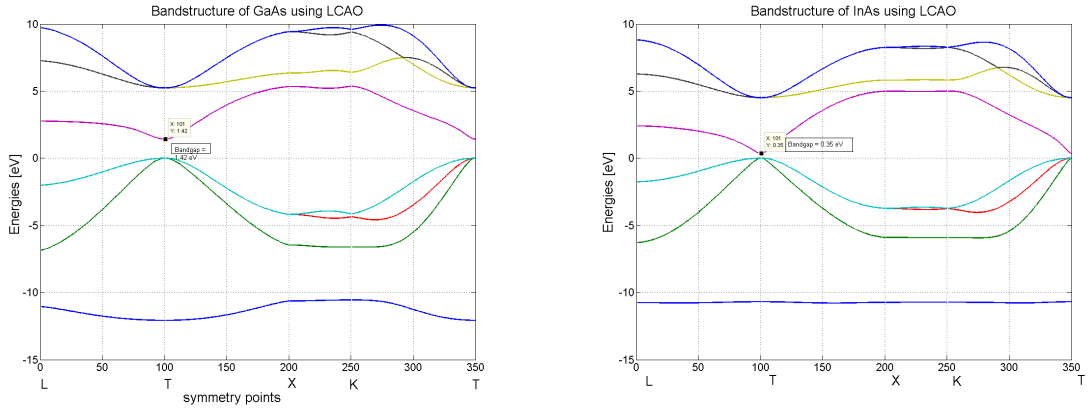

Figure 4.4: The bandstructures of GaAs and InAs at their equillibrium lattice constants, calculated using semi-empirical tight-binding parameters from [7]. We can see that although both InAs and GaAs are III-V semiconductors, the difference in band-gap (1.42 eV for GaAs vs. 0.35 eV for InAs) offers potential to tune the properties of a combined system.

result of this difference in bandstructure, the electronic and optical properties can be engineered by varying the composition of the crystal. With the length scale of a few nanometers, when one type of material (InAs) is completely surrounded by another (GaAs) in all directions, the electronic properties become 'zero-dimensional', and conduction electrons are confined in an electric potential well. These structures where electronic density is confined due to the arrangement of two types of crystals, are called quantum dots. Although these structures are called dots, they can also take pyramidal or other shapes depending on their growth process. Depending on the shape, size and composition of the quantum dot, properties such as photo-luminescence, and electrical conductivity can be controlled. For example, in the case of GaAs and InAs, epitaxial growth of one material on the other will result in a lattice mismatch strain, leading to and determining defect geometries and growth patterns. On the other hand, a boundary between two different semiconductors, creates a band-gap mismatch causing an electric potential gradient. In real systems, the interplay between strain-driven and gap-driven mismatch lead to a large variety of possibilities in growing and mixing various similar covalent compounds to create quantum dots. Quantum dots have been widely studied in recent years, with review articles on the subject [19] [58].

4.3.2 Setup

To investigate how the size of the InAs region in the GaAs matrix affects electron confinement, we investigate two possible formations of a quantum dot in a matrix of GaAs with a diameter of four nanometers or with a diameter of six nanometers. In both cases, the number of atoms and the underlying GaAs matrix are the same. The difference between the two cases is only that Ga atoms are replaced by In atoms, with accompanying differences in lattice constants and resulting mismatch.

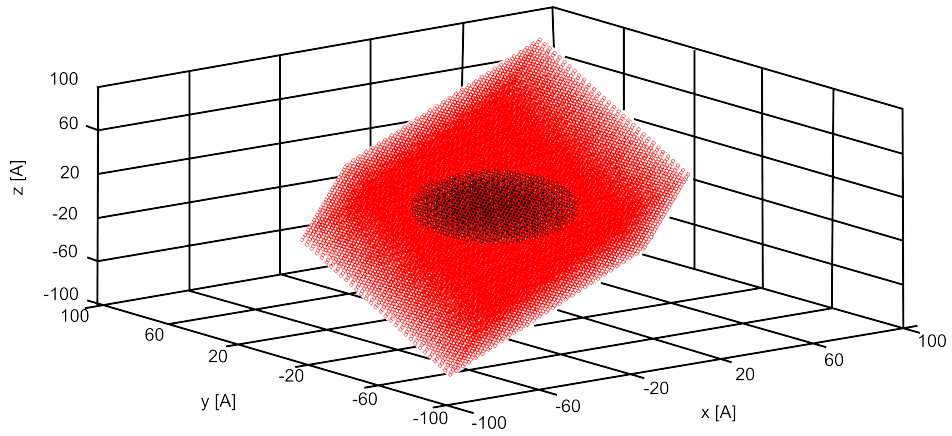

Figure 4.5: An atomistic representation of an InAs quantum dot in a GaAs matrix – a total of 60,000 atoms modeled using tight-binding.

4.4 Results

The computed local densities of states at the chemical potential, across the cross sectional plane of the InAs-GaAs matrix, are presented in figures 4.6a and 4.6b. Atomic resolution of the density of states at the Fermi level is important because electrons at the chemical potential are the most active in terms of reactivity and transport. We observe that the size of the proposed quantum dot determines electron confinement. When the quantum dot diameter is 6 nanometers, a higher concentration of electrons at the chemical potential is found inside the InAs region. On the other hand, if the proposed quantum dot is four nanometers, the electrons are not confined to a specific region.

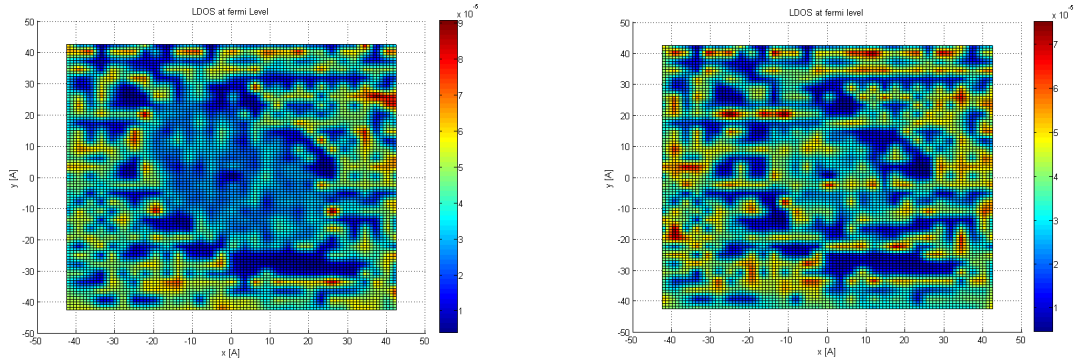

(a) Diameter of the quantum dot region is 6nm

(b) Diameter of the quantum dot is 4 nm.

Figure 4.6: Comparison of the local density of states in the cross section across the quantum dot, in two cases (a) when the quantum dot diameter is 6 nm, and (b) when the quantum dot nanometer is 4 nm. We can observe that the electron at the Fermi level is confined to the InAs region when the diameter is 6 nm.

4.5 Possible extension of the Kernel Polynomial Method

While the computation of static properties such as the local density of states for large systems is very useful, the Kernel Polynomial Method can be extended to compute excitation spectra, such as the total optical absorption rates seen in chapter 3, only at a larger scale. In this section, we first review the work that extends the Kernel Polynomial Method to 2-dimensions, and present its application to total optical absorption. Then, we present our own modification to this method that allows us to also compute the atomically resolved total optical absorption.

First, let us restate the total optical absorption rate:

$$W_{absorption}(\omega) = \sum_{k,q} |\langle q|H'|k\rangle|^2 \delta(E_k - E_q - \hbar\omega)(f_q - f_k) \tag{4.14}$$

where E_k and E_q represent different energy levels given by the Hamiltonian, f_q and f_k represent the Fermi-Dirac occupation at respective energies. The Kernel Polynomial Method approximation involves expressing $\delta(E_k - E_q - \hbar\omega)$ as a product of two $\delta()$ functions instead of one. Let us define a variation of the joint density of states:

$$J(x,y) = \sum_{k,q} |\langle q|H'|k\rangle|^2 \delta(x - E_q)\delta(y - E_k) \tag{4.15}$$

then, using the usual Kernel Polynomial approximation, this function $J(x,y)$ can be approximated by:

$$\tilde{J}(x,y) = \sum_{m,n} \frac{\mu_{mn} T_n(x) T_m(y)}{\pi^2 \sqrt{(1-x^2)(1-y^2)}} \tag{4.16}$$

We then calculate the relevant moments:

$$\mu_{mn} = \int\int J(x,y) T_n(x) T_m(x) dxdy \tag{4.17a}$$

$$\mu_{mn} = \int\int \sum_{k,q} |\langle q|H'|k\rangle|^2 \delta(x - E_q)\delta(y - E_k) T_n(x) T_m(x) dxdy \tag{4.17b}$$

$$= \sum_{k,q} |\langle q|H'|k\rangle|^2 \int\int \delta(x - E_q)\delta(y - E_k) T_n(x) T_m(x) dxdy \tag{4.17c}$$

$$= \sum_{k,q} \langle q|H'|k\rangle \langle k|H'|q\rangle T_n(E_q) T_m(E_k) \tag{4.17d}$$

Similar to the 1-D case, $E_q|q\rangle = \tilde{H}|q\rangle$, and since $T_n(E_q)$ is a linear combination of increasing powers of E_q, $\tilde{H}$ commutes.

$$\mu_{mn} = \sum_{k,q} \langle q|H' T_m(\tilde{H})|k\rangle \langle k|H' T_n(\tilde{H})|q\rangle \tag{4.17e}$$

Also, using $\sum_k |k\rangle \langle k| = 1$, we get:

$$\mu_{mn} = \sum_q \langle q|H'T_m(\tilde{H})H'T_n(\tilde{H})|q\rangle \tag{4.17f}$$

$$= Tr\left[H'T_m(\tilde{H})H'T_n(\tilde{H})\right] \tag{4.17g}$$

4.5.1 Atomistic projection of optical absorption

In this section, we present our modification to $W_{absorption}(\omega)$ and obtain atomistic contributions towards total optical absorption. From 4.14, we get

$$W_{absorption}(\omega) = \sum_{k,q} |\langle q|H'|k\rangle|^2 \delta(E_k - E_q - \hbar\omega)(f_q - f_k) \tag{4.18a}$$

If $x = E_k = y + \hbar\omega$ and $y = E_q$, and converting sum over q to integration over y, we get:

$$W_{absorption}(\omega) \simeq \int J(y + \hbar\omega, y)\left[f(y) - f(y + \hbar\omega)\right] dy \tag{4.18b}$$

The local absorption or emission calculations are an extension of this formulation. For this, we use the projection $\sum_{r\in\text{orbital basis}} |r\rangle \langle r| = 1$ to project out the lower energy bands, and we get:

$$W_{absorption}(\omega) = \sum_{k,q} \langle q|H'|k\rangle \langle k|H'|q\rangle \delta(E_k - E_q - \hbar\omega)(f_q - f_k) \tag{4.19a}$$

$$= \sum_{k,q} \langle q|H' \sum_r |r\rangle \langle r|\, k\rangle \langle k|H'|q\rangle \delta(E_k - E_q - \hbar\omega)(f_q - f_k) \tag{4.19b}$$

$$= \sum_r \left[\sum_{k,q} \langle q|H'\,|r\rangle \langle r|\, k\rangle \langle k|H'|q\rangle \delta(E_k - E_q - \hbar\omega)(f_q - f_k)\right] \tag{4.19c}$$

$$= \sum_r W_{absorption}(\omega, |r\rangle) \tag{4.19d}$$

Thus, we have defined a local rate of absorption by using the method of projection, $\sum_r |r\rangle \langle r| = 1$. For large systems, a method of Chebyshev polynomial moments can be then applied to calculate the local optical absorption.

$$W_{absorption}(\omega, |r\rangle) = \sum_{k,q} \langle q|H'\,|r\rangle \langle r|\, k\rangle \langle k|H'|q\rangle \delta(E_k - E_q - \hbar\omega)(f_q - f_k) \tag{4.20}$$

$$= \int_{-\infty}^{\infty}\int_{-\infty}^{\infty} J(x, y, r)\delta(E_x - Ey - \hbar\omega)dxdy \tag{4.21}$$

where similar to equation 4.16,

$$J(x, y, r) = \sum_{k,q} \langle q|H'|k\rangle \, \delta(x - E_q)\delta(y - E_k) \tag{4.22}$$

Using the usual Kernel Polynomial approximation, the function $J(x, y)$ can be approximated by:

$$\tilde{J}(x, y) = \sum_{m,n} \frac{\mu_{mn} T_n(x) T_m(y)}{\pi^2 \sqrt{(1 - x^2)(1 - y^2)}} \tag{4.23}$$

The moments of Chebyshev polynomial expansion are calculated in a similar fashion, such that

$$\mu_{mn} = \int_{-1}^{1} \int_{-1}^{1} J(x, y, r) T_n(x) T_m(y) dx dy \tag{4.24a}$$

$$\mu_{mn} = \int \int \sum_{k,q} \langle q|H'|r\rangle \, \langle r|k\rangle \, \langle k|H'|q\rangle \, \delta(x - E_q)\delta(y - E_k) T_n(x) T_m(y) dx dy \tag{4.24b}$$

$$= \sum_{k,q} \langle q|H'|r\rangle \, \langle r|k\rangle \, \langle k|H'|q\rangle \int \int \delta(x - E_q)\delta(y - E_k) T_n(x) T_m(y) dx dy \tag{4.24c}$$

$$\mu_{mn} = \sum_{k,q} \langle q|H'|r\rangle \, \langle r|k\rangle \, \langle k|H'|q\rangle \, T_n(E_q) T_m(E_k) \tag{4.24d}$$

Similar to what we did in the 1-D case, $E_q \, |q\rangle = \tilde{H} \, |q\rangle$, and since $T_n(E_q)$ is a linear combination of increasing powers of E_q, $\tilde{H}$ commutes, so that

$$\mu_{mn} = \sum_{k,q} \langle q|H'|r\rangle \, \langle r|T_m(E_k)|k\rangle \, \langle k|H' T_n(E_q)|q\rangle \tag{4.24e}$$

$$= \sum_{k,q} \langle r|T_m(\tilde{H})|k\rangle \, \langle k|H' T_n(\tilde{H})|q\rangle \, \langle q|H'|r\rangle \tag{4.24f}$$

Also, using $\sum_k |k\rangle \, \langle k| = 1$, and $\sum_q |q\rangle \, \langle q| = 1$ we get:

$$\mu_{mn} = \langle r|T_m(\tilde{H})|H' T_n(\tilde{H})|H'|r\rangle \tag{4.24g}$$

$$= \langle r|H' T_m(\tilde{H}) H' T_n(\tilde{H})|r\rangle = \langle r|T_m(\tilde{H}) H' T_n(\tilde{H}) H'|r\rangle \tag{4.24h}$$

Then, making the same approximations, i.e. if $x = E_k = y + \hbar\omega$ and $y = E_q$, and converting sum over q to integration over y, we get:

$$W_{holes}(r, \omega) \simeq \int J(y + \hbar\omega, y) \cdot [f(y) - f(y + \hbar\omega)] \, dy \tag{4.25}$$

We conclude this chapter by stating that while complete computations of the quantities mentioned above

are not yet finished, these methodological improvements facilitate the computation of atomically resolved optical absorption rates, and are applicable to systems larger than tens of thousands of atoms.

APPENDIX A

OPERATORS AND BRAKET NOTATION

In this chapter of the appendix, we elaborate on the use of braket notation, describe how observables can be written as operators, and how operators can be represented as matrices in given a basis. More details can be found in [13] [21] [22]

1. **Braket notation:**

   The braket notation is frequently used in quantum mechanics and physics. In a physical sense, the state of a system can be written as a function of the various positions of its particles, or all the possible positions of a single particle $\psi(r)$. The same system could also be defined in terms of the momentum it possesses, given by $\psi(\hbar\mathbf{k})$ where $\hbar k$ is the momentum of a free electron.Another alternative way to describe the system would be in terms of energy, in which case the wavefunction would be written as $\psi(E)$. In all cases, we are describing the same state, therefore, the 'ket' $|\psi\rangle$ is used to mean a quantum mechanical state in a general sense. Similarly, the 'bra' in 'braket'-notation, is its complementary conjugate. The interpretation of $\psi(r)$ is $\langle r|\psi\rangle$, and the interpretation of $\psi(\hbar\mathbf{k})$ is $\langle\hbar\mathbf{k}|\psi\rangle$. Similarly, $\psi^*(r) = \langle\psi|r\rangle$ and $\psi^*(\hbar\mathbf{k}) = \langle\psi|\hbar\mathbf{k}\rangle$

   One of the basic tenets of quantum mechanics is that the wavefunction of the system, ψ, has an interpretation of probability. Therefore,

   $$\langle\psi|\psi\rangle = \langle\psi| \int d^3r|r\rangle \langle r|\psi\rangle = \langle\psi| \int d^3k|k\rangle \langle k|\psi\rangle = 1 \tag{A.1}$$

   $$\langle\psi|\psi\rangle = \int d^3r|\psi(r)|^2 = \int d^3k|\psi(k)|^2 = 1 \tag{A.2}$$

   Here, we have introduced the idea of projection. Although the bases in this case were continuous, such as $\int d^3r\,|r\rangle\langle r| = 1$, other basis sets used in the thesis may be discrete, so that $\sum_i |\phi_i\rangle\langle\phi_i| = 1$.

2. **Operators:**

   An operator in quantum mechanics is similar to operators in differential equations, such as the laplacian ($\nabla^\mathbf{2}$), or the derivative ∇. In quantum mechanics, most observables can be written as operators that act on the wavefunction. For example, in classical mechanics, momentum is a measurable quantity, whereas in quantum mechanics, momentum has its own probabilistic distribution. For any state, if we

attempt to measure the momentum, there is an expected value and standard deviation. The expected value of the momentum is given by

$$\mathbf{p} = \frac{1}{2}\left(\langle\psi|i\hbar\nabla|\psi\rangle + \langle\psi| - i\hbar\nabla|\psi\rangle\right) \tag{A.3}$$

Here, although the momentum operator is $i\hbar\nabla$, we have to include the conjugate operator as well, because observables must be real quantities. Similarly, the kinetic-energy operator is given by $-\frac{\hbar^2}{2m}\nabla^2$, and the potential energy due to a classical charge is given by the Coulomb interaction term $\frac{1}{4\pi r}$. The expected kinetic energy and Coulomb energy are computed by using the same notation as we did for momentum.

3. **Matrix Algebra:** Above, we mentioned the calculation of kinetic energy, which can be written using braket-notation as follows

$$\langle\psi| - \frac{\hbar^2}{2m}\nabla^2|\psi\rangle \tag{A.4}$$

We also know that the wavefunction $\psi(r)$ can then be written as a linear combination of atomic orbitals. Given an orthogonal basis say, $\{\phi_k\}$, where $\langle\phi_i|\phi_j\rangle$ is defined by

$$\int d^3\mathbf{r}\phi_i^*(\mathbf{r})\phi_j(\mathbf{r}) = \delta_{i,j} \tag{A.5}$$

, we can expand the eigenstate of the Hamiltonian $\hat{H}\psi_i = E_i\psi_i$, as:

$$\psi_i(r) = \sum_k c_k^i \phi_k(r) \tag{A.6}$$

where the basis $\phi_k(r)$ and its behavior are well known. Then the Hamiltonian $\hat{H}$, or any other operator $\hat{O}$ can be written in matrix form. For example, given atomic orbitals $\phi_s(r)$ and $\phi_{px}(r)$, any physical quantity (denoted by an operator $\hat{O}$) has a matrix element O_{ij} associated with it so that:

$$O_{s,px} = \langle\phi_s|\hat{O}|\phi_{px}\rangle = \int \phi_s^*(r)\hat{O}\phi_{px}(r)dr \tag{A.7a}$$

As the number of atoms and the corresponding number of orbitals increases, the size of the matrix increases as well, with each term calculated as shown in A.7a. Thus, in electronic structure theory, the problem of calculating electronic eigenstates boils down to solving a matrix-eigenvalue problem where the Hamiltonian matrix is given by :

$$H_{ij} = \int \phi_i^*(r)\hat{H}\phi_j(r)dr \tag{A.7b}$$

And the eigenvalue equation to be solved is:

$$\hat{H} \left|\psi_\mu\right\rangle = E_\mu \left|\psi_\mu\right\rangle \tag{A.7c}$$

Above, the equation is written in terms of the operator $\hat{H}$, and the state $|\psi\rangle$ both of which are abstract concepts. In the following, we express the equation in matrix form. For that, we expand $|\psi\rangle$ as the sum of a linear combination of orbital basis, $|\psi_\mu\rangle = \sum_i c_i^\mu \phi_i$, we get:

$$\hat{H} \sum_i c_i^\mu \left|\phi_i\right\rangle = E_\mu \sum_i c_i^\mu \left|\phi_i\right\rangle \tag{A.7d}$$

Using $\langle\phi_j|$ on both sides, we get:

$$\left\langle\phi_j\right| \hat{H} \sum_i c_i^\mu \left|\phi_i\right\rangle = E_\mu \left\langle\phi_j\right| \sum_i c_i^\mu \left|\phi_i\right\rangle \tag{A.7e}$$

The operator $\hat{H}$ can be written as operators $\frac{\hbar^2}{2m}\nabla^2 - \frac{Ze^2}{4\pi r} + V_{xc}$ that act on $\psi(r) = \sum_i c_i \phi_i(r)$

$$\sum_i H_{ji} c_i^\mu = E_\mu \sum_i c_i^\mu \left\langle\phi_j|\phi_i\right\rangle \tag{A.7f}$$

Using $\langle\phi_j|\phi_i\rangle = \delta_{ij}$, the equation becomes:

$$\sum_i H_{ji} c_i^\mu = E_\mu \sum_i c_i^\mu \delta_{ij} \tag{A.7g}$$

This leads to the matrix eigenvalue equation of the form

$$\mathbf{Hc} = E\mathbf{c} \tag{A.7h}$$

APPENDIX B

DETERMINATION OF THE PERTURBATION HAMILTONIAN H'

In this chapter of the appendix, we first briefly outline the gauge transformations mentioned in chapter 3 of the thesis. These transformations connect different representations of the matter-field interaction. We then present preliminary details of computations for gallium(Ga) and arsenic(As) atoms. They are useful for possible future use in large heterogeneous unit cells such as quantum dots in GaAs matrix.

B.1 Hamiltonian transformations

For a system that includes charged particles and radiation, the total energy (expressed as the Hamiltonian) is given by:

$$H = \sum_{\alpha} \frac{1}{2} m_\alpha \mathbf{v}_\alpha^2 + \frac{\epsilon_0}{2} \int \mathbf{E}^2 + c^2 \mathbf{B}^2 dr \tag{B.1}$$

where $\mathbf{v}_\alpha$ is the particle velocity. In the presence of an applied external electric field (due to other charged particles or due to an applied electromagnetic field), we know that $\mathbf{v}_\alpha \neq \frac{\hbar}{i m_\alpha} \nabla$. Expressing the electric and magnetic fields in terms of the vector potential $\mathbf{A}$:

$$\mathbf{B}(\mathbf{r}, t) = \nabla \times \mathbf{A}(\mathbf{r}, t) \tag{B.2a}$$

$$\mathbf{E}(\mathbf{r}, t) = -\frac{\partial \mathbf{A}(\mathbf{r}, t)}{\partial t} - \nabla \phi(\mathbf{r}, t) \tag{B.2b}$$

from vector calculus, we realize that :

$$\nabla \cdot \mathbf{B}(\mathbf{r}, t) = \nabla \cdot \nabla \times \mathbf{A}(\mathbf{r}, t) = 0 \tag{B.3a}$$

$$\nabla \times \nabla \phi = 0 \tag{B.3b}$$

The above expressions are true for all gauges, thus from equation B.3a, we conclude that the magnetic field $\mathbf{B}$ is always transverse, and from equation B.3b that $\nabla\phi$ is always longitudinal. In Coulomb gauge, this is associated with the electric field due to a charged particle.

Given these observations, a conveneint choice of gauge is the Coulomb gauge $\nabla \cdot \mathbf{A} = 0$ so that $\mathbf{A}$ is purely

transverse. Then, the electric field is the sum of a transverse field, and a longitudinal field:

$$\mathbf{E} = \mathbf{E}^{\perp} + \mathbf{E}^{\parallel} \tag{B.4a}$$

$$\mathbf{E}^{\perp} = -\frac{\partial \mathbf{A}}{\partial t} \tag{B.4b}$$

$$\mathbf{E}^{\parallel} = -\nabla\phi \tag{B.4c}$$

This separation of the electric field into transverse and longitudinal fields is important because:

1. The longitudinal part of the electric field $\mathbf{E}^{\parallel}$, represents the Coulomb forces due to all charged particles in the system. Also, this does not have a direct time dependence, and is decoupled from any electromagnetic radiation that may be applied to the system, which is transverse.

2. The transverse part of the electric field depends on $\frac{\partial \mathbf{A}}{\partial t}$, so that for steady state approximations, the transverse electric field is $\mathbf{0}$, and becomes non-zero only when an oscillating field, such as electromagnetic radiation is produced or applied.

More detailed development is presented in [9]. Now that we have justified the use of the Coulomb gauge, the particle velocity in B.1 is related to the momentum $\frac{\hbar}{i}\nabla = \mathbf{p}$ such that:

$$\mathbf{v}_{\alpha} = \frac{1}{m_{\alpha}}\mathbf{p}_{\alpha} - q_{\alpha}\mathbf{A}(\mathbf{r}_{\alpha}, t) \tag{B.5}$$

In the equation above, the α indexes particle number, q is the charge of the particle and $\mathbf{A}$ is the vector field, which here is transverse. In a one-electron approximation, we get:

$$\mathbf{v} = \frac{1}{m}\mathbf{p} - q\mathbf{A}(\mathbf{r}, t) \tag{B.6}$$

Also, decomposing the electric field into its transverse and longitudinal parts, we obtain $\mathbf{E}^2$ of the Hamiltonian in B.1, as :

$$\mathbf{E}^2 = (\mathbf{E}^{\perp})^2 + (\mathbf{E}^{\parallel})^2 \tag{B.7}$$

where

$$\frac{\epsilon_0}{2}\int (\mathbf{E}^{\parallel})^2 = V_{Coulomb} \tag{B.8}$$

so that equation B.1 becomes:

$$\mathbf{H_{total}} = \frac{1}{2m}(\mathbf{p} - q\mathbf{A})^2 + V_{coulomb} + \frac{\epsilon_0}{2}\int \mathbf{E}^{\perp 2} + c^2\mathbf{B}^2 dr \tag{B.9a}$$

$$\mathbf{H_{total}} = \frac{1}{2m}(\mathbf{p} + e\mathbf{A})^2 + V_{coulomb} + \frac{\epsilon_0}{2}\int \mathbf{E}^{\perp 2} + c^2\mathbf{B}^2 dr \tag{B.9b}$$

$$\mathbf{H_{total}} = \frac{1}{2m}\mathbf{p}^2 + \frac{e}{2m}\mathbf{p}\cdot\mathbf{A} + \frac{e^2}{2m}\mathbf{A}^2 + V_{coulomb} + \frac{\epsilon_0}{2}\int \mathbf{E}^{\perp 2} + c^2\mathbf{B}^2 dr \tag{B.9c}$$

In the absence of applied electromagnetic radiation, $\mathbf{A} = 0$, $\mathbf{E}^{\perp} = 0$, and $\mathbf{B} = 0$ since they are all transverse fields, and ignoring spin degrees of freedom, the particle Hamiltonian is:

$$H_{particle} = \frac{1}{2m}\mathbf{p}^2 + V_{Coulomb} = H_{kinetic} + H_{Coulomb} \tag{B.10a}$$

Similarly, in absence of particles, only the electromagnetic radiation remains:

$$H_{rad} = \frac{\epsilon_0}{2}\int \mathbf{E}^{\perp 2} + c^2\mathbf{B}^2 dr \tag{B.10b}$$

The remaining terms, which are non-zero only when both particles and field exist, are interaction terms:

$$H_{int,1} = \frac{e}{m}\mathbf{p}\cdot\mathbf{A} \tag{B.10c}$$

$$H_{int,2} = \frac{e^2}{2m}\mathbf{A}^2 \tag{B.10d}$$

Therefore, the total Hamiltonian can be written as:

$$\mathbf{H_{total}} = H_{kinetic} + H_{Coulomb} + H_{rad} + H_{int,1} + H_{int,2} \tag{B.10e}$$

This total Hamiltonian can now undergo canonical transformations, so that we can observe and compute quantities more easily. The concept of canonical transformation is based on Lagrangian mechanics, according to which, different expressions of the Lagrangian, and their corresponding Hamiltonians are equivalent if the equations of motion remain unchanged. More details can be found in [31].

First, we describe the general procedure for a canonical transformation. Given an old Hamiltonian H_{old}, it can be transformed as follows:

$$H_{new} = e^{-iS}H_{old}e^{iS} \tag{B.11}$$

Expanding $e^{iS} = \sum_{n=0}^{\infty}\frac{(iS)^n}{n!} = 1 + iS + \frac{(iS)^2}{2!} + \frac{(iS)^3}{3!}$ and

$$e^{-iS} = \sum_{n=0}^{\infty}\frac{(-iS)^n}{n!} = 1 - iS + \frac{(-iS)^2}{2!} + \frac{(-iS)^3}{3!} + \dots \tag{B.12}$$

and then using commutation relations of the form:

$$[S, H_{old}] = SH_{old} - H_{old}S \tag{B.13}$$

The equation for B.11 can be rewritten as:

$$H_{new} = H_{old} - i[S, H_{old}] - \frac{1}{2!}[S, [S, H_{old}]] + \dots \tag{B.14}$$

$$S = \frac{1}{\hbar c} \int \mathbf{P} \cdot \mathbf{A} d^3 r \tag{B.15}$$

Where $\mathbf{P}$ is the polarizability vector field. Thus:

$$H_{new} = e^{-iS} H e^{iS} = H_{old} - i[S, H_{old}] - \frac{1}{2!}[S, [S, H_{old}]] + \dots \tag{B.16}$$

The choice of $S = \frac{1}{\hbar c} \int \mathbf{P} \cdot \mathbf{A} d^3 r$, makes this transformation the Power-Zineau transformation [4], [48].

B.1.1 Power-Zienau-Woolley transformation

In this transformation, terms beyond second order in B.16 cancel out to zero. We also note that [9] uses SI units, whereas [48] uses Gaussian units, but the result is the same. Carrying out this transformation ([4] and [48] contain full derivations), we get:

$$H_{particle,new} = H_{particle,old} - \frac{\epsilon_0}{2} \int \mu_0 \mathbf{m} \cdot \mathbf{b} d^3 r + H_{diamagn} - \frac{e}{m} \mathbf{p} \cdot \mathbf{A} + \frac{e^2}{2m} \mathbf{A}^2 \tag{B.17a}$$

$$H^{(1)}_{int,new} = H^{(1)}_{int,old} - \frac{e^2}{m} \mathbf{A}^2 = \frac{e}{m} \mathbf{p} \cdot \mathbf{A} - \frac{e^2}{m} \mathbf{A}^2 \tag{B.17b}$$

$$H^{(2)}_{int,new} = H^{(2)}_{int,old} = \frac{e^2}{2m} \mathbf{A}^2 \tag{B.17c}$$

$$H_{rad,new} = H_{rad,old} - \frac{\epsilon_0}{2} \int \frac{\mathbf{p}}{\epsilon_0} \cdot \mathbf{e}^{\perp} d^3 r + \frac{\epsilon_0}{2} \int |\frac{\mathbf{p}^{\perp}}{\epsilon_0}|^2 d^3 r \tag{B.17d}$$

Adding all of B.17a - B.17d, the $\mathbf{A}^2$ terms cancel out, and if we ignore the diamagnetic terms for now, we obtain:

$$H_{total} = H_{particle,old} + H_{rad,old} - \frac{\epsilon_0 \mu_0}{2} \int \mathbf{m} \cdot \mathbf{b} d^3 r - \frac{\epsilon_0}{2} \int \frac{\mathbf{p}}{\epsilon_0} \cdot (\mathbf{e}^{\perp} + \frac{\mathbf{p}^{\perp}}{\epsilon_0}) d^3 r \tag{B.18}$$

Therefore, our total Hamiltonian is now the sum of the older particle and field Hamiltonians, in addition to the new interaction tems, written in terms of the polarizability field ($\mathbf{p}(\mathbf{r})$) and the magnetization field ($\mathbf{m}(\mathbf{r})$), which depend on the charge distribution, and the electric and magnetic fields, which depend on the field and are gauge-invariant.

B.2 Polarizability field

In this section, we describe and compute the polarizability field mentioned in the previous section. For an assembly of charges assembled around a center $\mathbf{R_0}$, the polarizability field $\mathbf{P}(\mathbf{r})$ is defined as:

$$\mathbf{p}(\mathbf{r}) = \sum_{\alpha} e \int_0^1 q_\alpha \delta\left(\mathbf{r} - \lambda \mathbf{q}_\alpha\right) \mathrm{d}\lambda \tag{B.19a}$$

Where $\mathbf{q}_\alpha$ is the position of the $\alpha-$th particle. For a single particle case, $\mathbf{p}(\mathbf{r})$ can be written as :

$$\mathbf{p}(\mathbf{r}) = eq \int_0^1 \delta\left(\mathbf{r} - \lambda \mathbf{q}\right) \mathrm{d}\lambda \tag{B.19b}$$

Upto second order, the above equation can also be expanded in a series as follows

$$\mathbf{p}(\mathbf{r}) = -e(\mathbf{q} - \mathbf{r})\delta(\mathbf{r} - \mathbf{R_0}) + \frac{1}{2}e(\mathbf{q} - \mathbf{r})(\mathbf{q} - \mathbf{r})\nabla\delta(\mathbf{r} - \mathbf{R_0}) \tag{B.19c}$$

Here, $\mathbf{q}$ can also be interpreted as the position operator, in which case the expected value of $\mathbf{p(r)}$ is found. The first term is the series expansion is the dipole moment, and the second is the quadrupole moment. For atomic states $|\psi_{nlm}\rangle$ the polarizability field can be calculated as:

$$\mathbf{p}(\mathbf{R_0}) = \langle\psi_{nlm}| - e(\mathbf{q} - \mathbf{R_0}) + \frac{1}{2}e(\mathbf{q} - \mathbf{R_0})(\mathbf{q} - \mathbf{R_0})\nabla_r|\psi_{nlm}\rangle \tag{B.19d}$$

The first term, the dipole moment $\mu(\mathbf{R_0})$ is:

$$\mu(\mathbf{R_0}) = \langle\psi_{nlm}| - e(\mathbf{q} - \mathbf{R_0})|\psi_{nlm}\rangle \tag{B.20a}$$

$$= -e \int \psi^\star_{nlm}(\mathbf{q} - \mathbf{R_0})\psi_{nlm} d^3\mathbf{r} \tag{B.20b}$$

And the second term, the quadrupole moment is computed as:

$$Q(\mathbf{R_0}) = \frac{1}{2}e\,\langle\psi_{nlm}|(\mathbf{q} - \mathbf{R_0})(\mathbf{q} - \mathbf{R_0})\nabla_r|\psi_{nlm}\rangle \tag{B.21a}$$

For now, we can set $\mathbf{R_0} = \mathbf{0}$ then :

$$Q(\mathbf{R_0}) = \frac{1}{2}e\,\langle\psi_{nlm}|\mathbf{qq}\nabla_r|\psi_{nlm}\rangle \tag{B.21b}$$

where **qq** is a tensor operator equal to:

$$\mathbf{qq} = \begin{bmatrix} xx & \hat{xy} & xz \\ yx & yy & yz \\ zx & zy & zz \end{bmatrix} \tag{B.21c}$$

and

$$\nabla_r = \begin{bmatrix} \frac{d}{dx} \\ \frac{d}{dy} \\ \frac{d}{dz} \end{bmatrix} \tag{B.21d}$$

Therefore, the quadrupole moment is given by:

$$Q(\mathbf{R_0}) = \frac{1}{2} e \left\langle \psi_{nlm} \right| \begin{bmatrix} xx\frac{d}{dx} + xy\frac{d}{dy} + xz\frac{d}{dz} \\ yx\frac{d}{dx} + yy\frac{d}{dy} + yz\frac{d}{dz} \\ zx\frac{d}{dx} + zy\frac{d}{dy} + zz\frac{d}{dz} \end{bmatrix} \left| \psi_{nlm} \right\rangle \tag{B.21e}$$

$$= \frac{1}{2} e \begin{bmatrix} \int \psi^\star (xx\frac{d}{dx} + xy\frac{d}{dy} + xz\frac{d}{dz}) \psi d^3\mathbf{r} \\ \int \psi^\star (yx\frac{d}{dx} + yy\frac{d}{dy} + yz\frac{d}{dz}) \psi d^3\mathbf{r} \\ \int \psi^\star (zx\frac{d}{dx} + zy\frac{d}{dy} + zz\frac{d}{dz}) \psi d^3\mathbf{r} \end{bmatrix} \tag{B.21f}$$

The polarizability vector can thus be approximated to second order by the sum:

$$\mathbf{p}(\mathbf{R_0}) = \mu(\mathbf{R_0}) + Q(\mathbf{R_0}) \tag{B.22a}$$

. The polarizability vector can also be written in terms of its vector components

$$\mathbf{p}(\mathbf{R_0}) = \begin{bmatrix} p_x \\ p_y \\ p_z \end{bmatrix} = -e \begin{bmatrix} \int \psi^* x \psi \\ \int \psi^* y \psi \\ \int \psi^* z \psi \end{bmatrix} + \frac{1}{2} e \begin{bmatrix} \int \psi^\star (xx\frac{d}{dx} + xy\frac{d}{dy} + xz\frac{d}{dz}) \psi d^3\mathbf{r} \\ \int \psi^\star (yx\frac{d}{dx} + yy\frac{d}{dy} + yz\frac{d}{dz}) \psi d^3\mathbf{r} \\ \int \psi^\star (zx\frac{d}{dx} + zy\frac{d}{dy} + zz\frac{d}{dz}) \psi d^3\mathbf{r} \end{bmatrix} \tag{B.22b}$$

$$\begin{bmatrix} p_x \\ p_y \\ p_z \end{bmatrix} = -e \begin{bmatrix} \int \psi^\star \left(x - \frac{1}{2}(xx\frac{d}{dx} + xy\frac{d}{dy} + xz\frac{d}{dz}) \right) \psi d^3\mathbf{r} \\ \int \psi^\star \left(y - \frac{1}{2}(yx\frac{d}{dx} + yy\frac{d}{dy} + yz\frac{d}{dz}) \right) \psi d^3\mathbf{r} \\ \int \psi^\star \left(z - \frac{1}{2}(zx\frac{d}{dx} + zy\frac{d}{dy} + zz\frac{d}{dz}) \right) \psi d^3\mathbf{r} \end{bmatrix} \tag{B.22c}$$

If $\mathbf{E} = \begin{bmatrix} e_x \\ e_y \\ e_z \end{bmatrix}$ represents the applied transverse electric field, the interaction Hamiltonian is given by:

$$H_{pol,interaction} = \int d^3\mathbf{r}\mathbf{E} \cdot \mathbf{p}(\mathbf{r}) \tag{B.23}$$

which can be written as :

$$H_{pol,interaction} = ex \cdot px + ey \cdot py + ez \cdot pz \tag{B.24}$$

We now focus on the computation of the quantities px, py etc. As shown in the first chapter of the appendix, if ψ in equation B.22c were to be written as a linear combination of atomic orbitals, every quantity p_x, p_y, or p_z has a matrix associated it. We now present the simplest case, where the state ψ is a linear combination of two orbitals $|\phi_1\rangle$ and $|\phi_2\rangle$ so that every observable can be represented by a 2-by-2 matrix. For example, the $\mathbf{p}_x$ operator, polarizability field along x, is given by:

$$\mathbf{p_x} = -e \begin{bmatrix} \langle\phi_1|x|\phi_1\rangle - \frac{1}{2}\langle\phi_1|xx\frac{d}{dx} + xy\frac{d}{dy} + xz\frac{d}{dz}|\phi_1\rangle & \langle\phi_1|x|\phi_2\rangle - \frac{1}{2}\langle\phi_1|xx\frac{d}{dx} + xy\frac{d}{dy} + xz\frac{d}{dz}|\phi_2\rangle \\ \langle\phi_2|x|\phi_1\rangle - \frac{1}{2}\langle\phi_2|xx\frac{d}{dx} + xy\frac{d}{dy} + xz\frac{d}{dz}|\phi_1\rangle & \langle\phi_1|x|\phi_2\rangle - \frac{1}{2}\langle\phi_1|xx\frac{d}{dx} + xy\frac{d}{dy} + xz\frac{d}{dz}|\phi_2\rangle \end{bmatrix} \tag{B.25}$$

and so on for p_y and p_z matrix elements. let the matrix elements be written as $\mathbf{p}_x^{1\to2} = \langle\phi_1|\hat{p_x}|\phi_2\rangle$, so that:

$$\mathbf{p_x} = \begin{bmatrix} \mathbf{p}_x^{1\to1} & \mathbf{p}_x^{1\to2} \\ \mathbf{p}_x^{2\to1} & \mathbf{p}_x^{2\to2} \end{bmatrix} \tag{B.26}$$

Now, if we have two atoms A and B with atomic orbitals ϕ_s^A, ϕ_p^A, ϕ_s^B, and ϕ_p^B. The tight-binding Hamiltonian will look like:

$$H_0 = \begin{pmatrix} E_s^A & 0 & E_{ss} & E_{sp} \\ 0 & E_p^A & E_{ps} & E_{pp} \\ E_{ss} & E_{sp} & E_s^B & 0 \\ E_{ps} & E_{pp} & 0 & E_p^B \end{pmatrix} \tag{B.27}$$

and the polarizability matrix along x-axis ($\mathbf{P_x}$) will be of the 4-by-4 matrix form:

$$P_x = \begin{pmatrix} 0 & a & b & b \\ a & 0 & b & b \\ b & b & 0 & a \\ b & b & a & 0 \end{pmatrix} \tag{B.28}$$

B.3 Calculation of electric and magnetic dipoles $\langle\psi_i|\,\mathbf{r}\cdot\mathbf{E}\,|\psi_j\rangle$ and $\langle\psi_i|\,\mathbf{m}\cdot\mathbf{B}\,|\psi_j\rangle$

In this section, we now present numerical calculations for specific atomic orbitals of gallium and arsenic atoms. For now, our computation is limited to the dipole approximation, although higher orders of the polarizability field can be computed using methods discussed in the section above.

B.3.1 The electric dipole contribution $\langle\psi_i|\,\mathbf{r}\cdot\mathbf{E}\,|\psi_j\rangle$

We recall that in the dipole approximation, the vector operator $\mathbf{r}$ can be described using three different scalar operators $\hat{x}$, $\hat{y}$ and $\hat{z}$ in Cartesian coordinates:

$$\langle\psi_i|\,\mathbf{r}\,|\psi_j\rangle = \begin{bmatrix}\langle\psi_i|\,\hat{x}\,|\psi_j\rangle\\ \langle\psi_i|\,\hat{y}\,|\psi_j\rangle\\ \langle\psi_i|\,\hat{z}\,|\psi_j\rangle\end{bmatrix} \tag{B.29}$$

For a system with N atoms, each possible eigenstate ψ_{TB} is represented by a linear combination of atomic orbitals, with coefficients given by $\mathbf{C}$.

$$\psi_{TB} = \sum_i C_i\phi_i \tag{B.30}$$

$$= [C_1\phi_s + C_2\phi_{px} + C_3\phi_{py} + C_4\phi_{pz}]_{atom1} + [C_5\phi_s + C_6\phi_{px} + C_7\phi_{py} + C_8\phi_{pz}]_{atom2} + \dots \tag{B.31}$$

$$= \begin{bmatrix}C1\\ C2\\ C3\\ C4\\ C5\\ .\\ .\\ .\\ .\end{bmatrix} \cdot \begin{pmatrix}\phi_1\\ \phi_2\\ \phi_3\\ \phi_4\\ \phi_5\\ .\\ .\\ .\\ .\end{pmatrix} \tag{B.32}$$

The coefficients C_i are given by the eigenvectors of the Hamiltonian, which itself is obtained by using Slater Koster parameters in tight-binding theory. Then given two eigenstates $|\psi_f\rangle$ and $|\psi_i\rangle$, the calculation of $\langle\psi_f|\,\hat{x}\,|\psi_i\rangle$, which is required to compute transition rates or optical absorption or other related quantites, can be done by first decoupling the expression as follows:

$$\langle\psi_f|\,\hat{x}\,|\psi_i\rangle = \langle\sum_j C_j^*\phi_j|\,\hat{x}\,|\sum_i C_i\phi_i\rangle = \sum_{i,j} C_j^*C_i\,\langle\phi_j|\,\hat{x}\,|\phi_i\rangle \tag{B.33}$$

The above equation can also be simplified into:

$$\langle\psi_f|\,\hat{x}\,|\psi_i\rangle =$$

$$\begin{bmatrix} C_1 & C_2 & C_3 & C4 & . & . & . \end{bmatrix}_f^* \cdot \begin{bmatrix} \langle\phi_1|\,x\,|\phi_1\rangle & \langle\phi_1|\,x\,|\phi_2\rangle & \langle\phi_1|\,x\,|\phi_3\rangle & \langle\phi_1|\,x\,|\phi_4\rangle & . & . & . & . \\ \langle\phi_2|\,x\,|\phi_1\rangle & \langle\phi_2|\,x\,|\phi_2\rangle & \langle\phi_2|\,x\,|\phi_3\rangle & \langle\phi_2|\,x\,|\phi_4\rangle & . & . & . & . \\ \langle\phi_3|\,x\,|\phi_1\rangle & \langle\phi_3|\,x\,|\phi_2\rangle & \langle\phi_3|\,x\,|\phi_3\rangle & \langle\phi_3|\,x\,|\phi_4\rangle & . & . & . & . \\ \langle\phi_4|\,x\,|\phi_1\rangle & \langle\phi_4|\,x\,|\phi_2\rangle & \langle\phi_4|\,x\,|\phi_3\rangle & \langle\phi_4|\,x\,|\phi_4\rangle & . & . & . & . \\ . & . & . & . & . & . & . & . \\ . & . & . & . & . & . & . & . \\ . & . & . & . & . & . & . & . \end{bmatrix} \cdot \begin{bmatrix} C_1 \\ C_2 \\ C_3 \\ C4 \\ . \\ . \\ . \end{bmatrix}_i \tag{B.34}$$

The vectors composed of $\begin{bmatrix} C_1 & C_2 & \dots \end{bmatrix}_f$ and $\begin{bmatrix} C_1 \\ C_2 \\ \dots \end{bmatrix}_i$ corresponding to $|\psi\rangle_f$ and $|\psi\rangle_i$ respectively, are obtained by diagonalizing the tight-binding Hamiltonian, or other alternative methods. Computing the matrix above, whose elements are of the type $\langle\phi_1|x|\phi_2\rangle$ will be the concern of the following sections.

B.4 Slater orbitals and basis used in tight-binding

We know that ϕ_i used in tight-binding can be written as a product of the radial and angular components, as follows :

$$\mathbf{\Phi}(r,\theta,\phi) = R(r)\cdot T(\theta,\phi) \tag{B.35}$$

Notation change : Whenever there are two ϕ's here, the bold-upper case $\mathbf{\Phi}$ represents the atomic orbital whereas the smaller case ϕ is just the angle. Usually, only one is used, and the interpretation is obvious by context.

The radial part can be thought of as a modified form of the eigenfunctions of radial part of the Schrodinger equation of an atom, and take the following form:

$$R_{nl}(r) = \frac{r^{n-1}}{\sqrt{(2n)!}}[C_1(2\eta_1)^{n+\frac{1}{2}}\,e^{-\eta_1 r} + C_2(2\eta_2)^{n+\frac{1}{2}}\,e^{-\eta_2 r}] \tag{B.36}$$

where the coefficients C_1, η_1, C_2, η_2 for GaAs are as follows:

Gallium:

Orbital	C_1	η_1	C_2	η_2
s	2.041	0.662	0	0
p	1.616	0.705	5.835	0.596
d	1.028	0.636	0	0

Arsenic:

Orbital	C_1	η_1	C_2	η_2
s	2.344	0.634	0	0
p	2.102	0.753	7.588	0.539
d	0.918	0.660	3.926	0.681

Similarly, the angular parts of the orbitals are spherical harmonics that are defined by:

$$Y_l^m(\theta,\phi) = (-1)^m \sqrt{\frac{(2l+1)}{4\pi}\frac{(l-|m|)!}{(l+|m|)!}} e^{im\phi} P_l^m \cos\theta \tag{B.37}$$

Where P_l^m are the Legendre polynomials. The spherical harmonics relevant to our orbitals (s, p, d) or (l = 0, 1, 2) and for every value of l, m_l values, the z-component of angular momentum can range from -l, -l+1, ..., l-1, l. l = 0 or s-orbitals:

$$Y_0^0 = \sqrt{\frac{1}{4\pi}} \tag{B.38a}$$

l = 1, spherical harmonics that make up p-orbitals:

$$Y_1^{\pm 1} = \mp\sqrt{\frac{3}{8\pi}} \sin\theta e^{\pm i\phi} \tag{B.38b}$$

$$Y_1^0 = \sqrt{\frac{3}{4\pi}} \cos\theta \tag{B.38c}$$

l = 2, spherical harmonics that make up d-orbitals:

$$Y_2^0 = \sqrt{\frac{5}{16\pi}}(3\cos^2\theta - 1) \tag{B.38d}$$

$$Y_2^{\pm 1} = \mp\sqrt{\frac{15}{8\pi}} \sin\theta\cos\theta e^{\pm i\phi} \tag{B.38e}$$

$$Y_2^{\pm 2} = \sqrt{\frac{15}{32\pi}} \sin^2\theta e^{\pm 2i\phi} \tag{B.38f}$$

The Slater orbitals are given in terms of s, px, py, pz, dxy, dyz, dzx ... orbitals. These can be expressed as the linear combinations of the angular spherical harmonics:

$$|s\rangle = R_{40}(r) Y_0^0 \tag{B.39a}$$

$$|px\rangle = R_{41}(r) \frac{Y_1^1 + Y_1^{-1}}{\sqrt{2}} \tag{B.39b}$$

$$|py\rangle = R_{41}(r) \frac{Y_1^1 - Y_1^{-1}}{i\sqrt{2}} \tag{B.39c}$$

$$|pz\rangle = R_{41}(r) Y_1^0 \tag{B.39d}$$

$$|d_{xy}\rangle = R_{32}(r)\frac{Y_2^2 - Y_2^{-2}}{i\sqrt{2}} \tag{B.39e}$$

$$|d_{yz}\rangle = R_{32}(r)\frac{Y_2^1 + Y_2^{-1}}{i\sqrt{2}} \tag{B.39f}$$

$$|d_{zx}\rangle = R_{32}(r)\frac{Y_2^1 + Y_2^{-1}}{\sqrt{2}} \tag{B.39g}$$

$$|d_{x^2-y^2}\rangle = R_{32}(r)\frac{Y_2^2 + Y_2^{-2}}{\sqrt{2}} \tag{B.39h}$$

$$|d_{z^2}\rangle = R_{32}(r)Y_2^0 \tag{B.39i}$$

Above, R_{nl} represents the radial part of the wavefunction, where n is given by its position (row) in the periodic table. l, which represents the total angular momentum of that orbital, and Y_l^m which is the angular part of the wavefunction have been described previously.

B.4.1 Integrations for individual components of electric dipole moment $\tilde{\mathbf{X}}_{\mathbf{ij}} = \langle\phi_i| x |\phi_j\rangle$.

As an example, let us try calculating the component $\mathbf{X}_{s-px}^{Ga}$, defined as the x-component of dipole moment between s and px orbitals of gallium atom:

$$\langle\phi_s| x |\phi_{px}\rangle^{Ga} = \int_0^{2\pi}\int_0^{\pi}\int_0^{\infty} \left(R_s^{Ga}(r)Y_s^{Ga}(\theta,\phi)\right) x \left(R_{px}^{Ga}(r)Y_{px}^{Ga}(\theta,\phi)\right) r^2 \sin\theta dr d\theta d\phi \tag{B.40a}$$

$$= \int_0^{2\pi}\int_0^{\pi}\int_0^{\infty} \left(R_s^{Ga}(r)Y_0^0\right) (r\sin\theta\cos\phi)\, R_{px}^{Ga}(r) \left(\frac{Y_1^1 + Y_{1^-1}}{\sqrt{2}}\right) r^2 \sin\theta dr d\theta d\phi \tag{B.40b}$$

$$= \int_0^{2\pi}\int_0^{\pi} Y_0^0 \sin\theta\cos\phi \left(\frac{Y_1^1 + Y_{1^-1}}{\sqrt{2}}\right) \sin\theta d\theta d\phi \int_0^{\infty} r^3 R_s^{Ga}(r) R_{px}^{Ga}(r) dr \tag{B.40c}$$

The radial components are expressed in terms of Slater components as shown in B.36 so we get:

$$\langle\phi_s| x |\phi_{px}\rangle^{Ga} = \int_0^{\infty} \frac{r^{n-1} r^3 r^{n-1}}{\sqrt{(2n)!(2n)!}} \left(C_1^{'}(2\eta_1^{'})^{n+\frac{1}{2}} e^{-\eta_1^{'} r} + C_2(2\eta_2^{'})^{n+\frac{1}{2}} e^{-\eta_2^{'} r}\right) \cdot$$

$$\left(C_1(2\eta_1)^{n+\frac{1}{2}} e^{-\eta_1 r} + C_2(2\eta_2)^{n+\frac{1}{2}} e^{-\eta_2 r}\right) dr \tag{B.40d}$$

B.4.2 Results of integration

The matrix representation for dipole moments within gallium atom are given by:

$$|X| =$$

$$\begin{bmatrix} |\langle s|x|s\rangle|_{Ga} & |\langle s|x|px\rangle|_{Ga} & |\langle s|x|py\rangle|_{Ga} & |\langle s|x|pz\rangle|_{Ga} & 0 & |\langle s|x|d_{xy}\rangle|_{Ga} & |\langle s|x|d_{yz}\rangle|_{Ga} & . & . \\ |\langle px|x|s\rangle|_{Ga} & |\langle px|x|px\rangle|_{Ga} & |\langle px|x|py\rangle|_{Ga} & |\langle px|x|pz\rangle|_{Ga} & 0 & |\langle px|x|d_{xy}\rangle|_{Ga} & |\langle px|x|d_{yz}\rangle|_{Ga} & . & . \\ |\langle py|x|s\rangle|_{Ga} & |\langle py|x|px\rangle|_{Ga} & |\langle py|x|py\rangle|_{Ga} & |\langle py|x|pz\rangle|_{Ga} & 0 & |\langle py|x|d_{xy}\rangle|_{Ga} & |\langle py|x|d_{yz}\rangle|_{Ga} & . & . \\ |\langle pz|x|s\rangle|_{Ga} & |\langle pz|x|px\rangle|_{Ga} & |\langle pz|x|py\rangle|_{Ga} & |\langle pz|x|pz\rangle|_{Ga} & 0 & |\langle pz|x|d_{xy}\rangle|_{Ga} & |\langle pz|x|d_{yz}\rangle|_{Ga} & . & . \\ . & . & . & . & . & . & . & . & \\ . & . & . & . & . & . & . & . & \\ . & . & . & . & . & . & . & . & \end{bmatrix} \tag{B.41}$$

The numerical values of these integrations, carried out according to the previous section are now inserted, so that we obtain the matrix for the x-component of the electric dipole for gallium atom.

$$= \begin{pmatrix} |s\rangle & |px\rangle & |py\rangle & |pz\rangle & |s^*\rangle & |d_{xy}\rangle & |d_{yz}\rangle & |d_{zx}\rangle & |d_{x^2-y^2}\rangle & |d_{z^2-r^2}\rangle \\ 0.2242 & 0.0013 & 617.1703 & 0.0000 & 0 & 0.0015 & 0.0000 & 0.0000 & 0.2338 & 0.0450 \\ 0.0013 & 0.0000 & 0.0029 & 0.0000 & 0 & 419.0421 & 0.0000 & 0.0000 & 0.0018 & 0.0005 \\ 617.1703 & 0.0029 & 0.9332 & 0.0000 & 0 & 0.0035 & 0.0000 & 0.0000 & 418.4828 & 241.7726 \\ 0.0000 & 0.0000 & 0.0000 & 0.3111 & 0 & 0.0000 & 418.7625 & 0.0009 & 0.0000 & 0.0000 \\ 0.0015 & 419.0421 & 0.0035 & 0.0000 & 0 & 0.0000 & 0.0000 & 0.0000 & 0.0035 & 0.0012 \\ 0.0000 & 0.0000 & 0.0000 & 418.7625 & 0 & 0.0000 & 0.4458 & 0.0014 & 0.0000 & 0.0000 \\ 0.0000 & 0.0000 & 0.0000 & 0.0009 & 0 & 0.0000 & 0.0014 & 0.0000 & 0.0000 & 0.0000 \\ 0.2338 & 0.0018 & 418.4828 & 0.0000 & 0 & 0.0035 & 0.0000 & 0.0000 & 0.5573 & 0.1930 \\ 0.0450 & 0.0005 & 241.7726 & 0.0000 & 0 & 0.0012 & 0.0000 & 0.0000 & 0.1930 & 0.1858 \end{pmatrix} \tag{B.42}$$

Similarly, the matrix elements for the y and z-components of the electric dipole moment of gallium are:

$$|Y| =$$

$$\begin{bmatrix} |s\rangle & |px\rangle & |py\rangle & |pz\rangle & |s^*\rangle & |d_{xy}\rangle & |d_{yz}\rangle & |d_{zx}\rangle & |d_{x^2-y^2}\rangle & |d_{z^2-r^2}\rangle \\ 0.0007 & 617.5824 & 0.0013 & 0.0000 & 0 & 0.0000 & 0.0000 & 0.0000 & 0.0007 & 0.0001 \\ 617.5824 & 0.0000 & 0.0000 & 0.0000 & 0 & 0.0000 & 0.0000 & 0.0000 & 419.0421 & 241.9341 \\ 0.0013 & 0.0000 & 0.0029 & 0.0000 & 0 & 419.0421 & 0.0000 & 0.0000 & 0.0018 & 0.0005 \\ 0.0000 & 0.0000 & 0.0000 & 0.0010 & 0 & 0.0000 & 0.0009 & 419.0421 & 0.0000 & 0.0000 \\ 0.0000 & 0.0000 & 419.0421 & 0.0000 & 0 & 0.0000 & 0.0000 & 0.0000 & 0.0000 & 0.0000 \\ 0.0000 & 0.0000 & 0.0000 & 0.0009 & 0 & 0.0000 & 0.0014 & 0.0000 & 0.0000 & 0.0000 \\ 0.0000 & 0.0000 & 0.0000 & 419.0421 & 0 & 0.0000 & 0.0000 & 0.0000 & 0.0000 & 0.0000 \\ 0.0007 & 419.0421 & 0.0018 & 0.0000 & 0 & 0.0000 & 0.0000 & 0.0000 & 0.0018 & 0.0006 \\ 0.0001 & 241.9341 & 0.0005 & 0.0000 & 0 & 0.0000 & 0.0000 & 0.0000 & 0.0006 & 0.0006 \end{bmatrix} \tag{B.43}$$

$$|Z| =$$

$\|s\rangle$	$\|px\rangle$	$\|py\rangle$	$\|pz\rangle$	$\|s^*\rangle$	$\|d_{xy}\rangle$	$\|d_{yz}\rangle$	$\|d_{zx}\rangle$	$\|d_{x^2-y^2}\rangle$	$\|d_{z^2-r^2}\rangle$
0.0007	0.0000	0.0000	617.3748	0	0.0000	0.1558	0.0005	0.0000	0.0011
0.0000	0.0000	0.0000	0.0010	0	0.0000	0.0009	419.0421	0.0000	0.0000
0.0000	0.0000	0.0000	0.3111	0	0.0000	418.7625	0.0009	0.0000	0.0000
617.3748	0.0010	0.3111	0.0039	0	0.0009	0.0000	0.0000	0.1398	483.7037
0.0000	0.0000	0.0000	0.0009	0	0.0000	0.0014	0.0000	0.0000	0.0000
0.1558	0.0009	418.7625	0.0000	0	0.0014	0.0000	0.0000	0.2229	0.1287
0.0005	419.0421	0.0009	0.0000	0	0.0000	0.0000	0.0000	0.0007	0.0004
0.0000	0.0000	0.0000	0.1398	0	0.0000	0.2229	0.0007	0.0000	0.0000
0.0011	0.0000	0.0000	483.7037	0	0.0000	0.1287	0.0004	0.0000	0.0037

(B.44)

The same quantities can also be computed for arsenic atom, and for inter-atomic contributions. As a result, we obtain the matrix representation of the x-component of the electric dipole moment:

$$x = \begin{pmatrix} X_{Ga-Ga} & X_{Ga-As} \\ X_{As-Ga} & X_{As-As} \end{pmatrix} \tag{B.45}$$

Here the two diagonal matrices X_{Ga-Ga} and X_{As-As} can be calculated as shown. Next, if we want, we could obtain the cross diagonal elements using slater two center integrals, but they can be smaller in magnitude than the diagonal ones by three orders of magnitude. Thus, this matrix can now be used in equation B.34 to compute the x-component of the dipole associated with two energy levels. Similarly, the y and z-compoents of the dipole moments of a quantum mechanical state, or possible transitions, can be computed by using a combination of the above matrix formalism and equation B.34.

B.4.3 The magnetic dipole contribution $\langle\psi_i|\,\mathbf{m}\cdot\mathbf{B}\,|\psi_j\rangle$

In this subsection, we present preliminary analysis for computing the magnetic dipole moments. The framework for relating the magnetic dipole contribution to tight-binding results is very similar to the one used to compute the electric dipole. The electric dipole vector operator $\hat{\mathbf{r}}$ is replaced by the magnetic moment operator $\mathbf{m}$ which, when dotted with the magnetic field instead of the electric field, gives the interaction Hamiltonian contribution. A similar decomposition of $\mathbf{m}$ into 3 Cartesian scalar operators as follows:

$$\langle\psi_i|\,\mathbf{m}\,|\psi_j\rangle = \begin{bmatrix} \langle\psi_i|\,\hat{m_x}\,|\psi_j\rangle \\ \langle\psi_i|\,\hat{m_y}\,|\psi_j\rangle \\ \langle\psi_i|\,\hat{m_z}\,|\psi_j\rangle \end{bmatrix} \tag{B.46}$$

Like in the electric dipole case, each of $\langle\psi_i|\,\hat{m_x}\,|\psi_j\rangle$, $\langle\psi_i|\,\hat{m_y}\,|\psi_j\rangle$ and $\langle\psi_i|\,\hat{m_z}\,|\psi_j\rangle$ can be written as matrices. Let us assume that $\tilde{\mathbf{M}}_{\mathbf{x}}$ represents the x-component of the magnetic dipole moment.

If we are to calculate the magnetic moment however, we must also consider the magnetic moments due to spin, so instead of using spin-degenerate orbitals (using one set of $|nlm\rangle$ atomic orbitals, and multiplying by 2 to account for two spins), we have to use their corresponding spins as well. Then, we can define:

$$\tilde{\mathbf{M}}_{\mathbf{x}} = \begin{bmatrix} \langle\phi_1|\,m_x\,|\phi_1\rangle & \langle\phi_1|\,m_x\,|\phi_2\rangle & \langle\phi_1|\,m_x\,|\phi_3\rangle & \langle\phi_1|\,m_x\,|\phi_4\rangle & . & . & . & . \\ \langle\phi_2|\,m_x\,|\phi_1\rangle & \langle\phi_2|\,m_x\,|\phi_2\rangle & \langle\phi_2|\,m_x\,|\phi_3\rangle & \langle\phi_2|\,m_x\,|\phi_4\rangle & . & . & . & . \\ \langle\phi_3|\,m_x\,|\phi_1\rangle & \langle\phi_3|\,m_x\,|\phi_2\rangle & \langle\phi_3|\,m_x\,|\phi_3\rangle & \langle\phi_3|\,m_x\,|\phi_4\rangle & . & . & . & . \\ \langle\phi_4|\,m_x\,|\phi_1\rangle & \langle\phi_4|\,m_x\,|\phi_2\rangle & \langle\phi_4|\,m_x\,|\phi_3\rangle & \langle\phi_4|\,m_x\,|\phi_4\rangle & . & . & . & . \\ . & . & . & . & . & . & . & . \\ . & . & . & . & . & . & . & . \\ . & . & . & . & . & . & . & . \end{bmatrix} \tag{B.47}$$

where ϕ_i represents the ith atomic orbital (which now also include up or down spins) used in tight-binding calculation.

The magnetic moment operator in any direction is defined in terms of its orbital and spin angular momenta as follows

$$m_x = -\mu_B \frac{\left(g_l \hat{L_x} + g_s \hat{S_x}\right)}{\hbar} \tag{B.48}$$

Here, $\mu_B = \frac{e\hbar}{2m_e}$ is a constant called the 'Bohr magneton', and is equal to $5.79 * 10^{-5} eV/T$, the coefficient g's depend on the particle and the type of angular momentum. For orbital angular momentum of an electron, $g_l = 1$ and for spin angular momentum, $g_s = 2.00232$. So the matrix component $\tilde{\mathbf{Mx}}_{\mathbf{ij}}$ can be calculated with the integrals:

$$Mx_{ij} = \langle\phi_j|\,m_x\,|\phi_i\rangle = -\frac{\mu_B}{\hbar} \cdot \left(\int \phi_j^* \hat{L_x} \phi_i dV + 2 \cdot \langle\phi_j|\,\hat{S_x}\,|\phi_i\rangle \right) \tag{B.49}$$

As in the case of electric dipole moment, we expect the orbital angular momentum and spin angular momentum values to be the greatest between orbitals of an individual atom, smaller for nearest neighbor atoms, and 0 for orbitals located on distant atoms.

REFERENCES

[1] Peter M Albrecht and Joseph W Lyding. Lateral Manipulation of Single Walled Carbon Nanotubes on H Passivated Si(100) Surfaces with an UltrahighVacuum Scanning Tunneling Microscope. *Small*, 3(1):146–152, 2007.

[2] Juan Alonso. Lecture notes in AA 222. *Aerospace Design Lab, Stanford University*, 2010.

[3] Neil W Ashcroft and N David Mermin. *Solid State Physics*. Brooks Cole, 1976.

[4] M Babiker, EA Power, and T Thirunamachandran. On a generalization of the power-zienau-woolley transformation in quantum electrodynamics and atomic field equations. *Proceedings of the Royal Society of London. A. Mathematical and Physical Sciences*, 338(1613):235–249, 1974.

[5] Richard Balog, Bjarke Jørgensen, Justin Wells, Erik Lægsgaard, Philip Hofmann, Flemming Besenbacher, and Liv Hornekær. Atomic hydrogen adsorbate structures on graphene. *Journal of the American Chemical Society*, 131(25):8744–8745, 2009.

[6] Timothy B Boykin, Gerhard Klimeck, and Fabiano Oyafuso. Valence band effective-mass expressions in the sp^3 d^5 s* empirical tight-binding model applied to Si and Ge parametrization. *Physical Review B*, 69(11):115201, 2004.

[7] DJ Chadi and ML Cohen. Tight-binding calculations of the valence bands of diamond and zincblende crystals. *Physica Status Solidi (b)*, 68(1):405–419, 1975.

[8] Shun Lien Chuang. *Physics of Optoelectronic Devices*. Wiley New York, 1995.

[9] Claude Cohen-Tannoudji, Jacques Dupont-Roc, and Gilbert Grynberg. *Photons and Atoms: Introduction to Quantum Electrodynamics*. Wiley Online Library, 1997.

[10] Andrew R Conn, Katya Scheinberg, and Luis N Vicente. *Introduction to Derivative-free Optimization*, volume 8. Society for Industrial and Applied Mathematics, 2009.

[11] DC Elias, RR Nair, TMG Mohiuddin, SV Morozov, P Blake, MP Halsall, AC Ferrari, DW Boukhvalov, MI Katsnelson, AK Geim, et al. Control of graphene's properties by reversible hydrogenation: evidence for graphane. *Science*, 323(5914):610–613, 2009.

[12] Marcus Elstner, Dirk Porezag, G Jungnickel, J Elsner, M Haugk, Th Frauenheim, Sandor Suhai, and Gotthard Seifert. Self-consistent-charge density-functional tight-binding method for simulations of complex materials properties. *Physical Review B*, 58(11):7260, 1998.

[13] Sverre Froyen and Walter A Harrison. Elementary prediction of linear combination of atomic orbitals matrix elements. *Physical Review B*, 20(6):2420, 1979.

[14] Haili Gao, Lu Wang, Jijun Zhao, Feng Ding, and Jianping Lu. Band gap tuning of hydrogenated graphene: H coverage and configuration dependence. *The Journal of Physical Chemistry C*, 115(8):3236–3242, 2011.

[15] Stefan Goedecker and L Colombo. Efficient linear scaling algorithm for tight-binding molecular dynamics. *Physical Review Letters*, 73(1):122, 1994.

[16] David E Goldberg. *Genetic Algorithm in Search, Optimization and Machine Learning, Addison*, volume 1. Wesley Publishing Company, Reading, MA, 1989.

[17] David Jeffrey Griffiths and Edward G Harris. *Introduction to Quantum Mechanics*, volume 2. Prentice Hall New Jersey, 1995.

[18] Melinda Y Han, Barbaros Özyilmaz, Yuanbo Zhang, and Philip Kim. Energy band-gap engineering of graphene nanoribbons. *Physical Review Letters*, 98(20):206805, 2007.

[19] K Hannewald, S Glutsch, and F Bechstedt. Theory of photoluminescence in semiconductors. *Physical Review B*, 62(7):4519, 2000.

[20] Walter A Harrison. *Solid State Theory*. Courier Corporation, 1970.

[21] Walter A Harrison. Total energies in the tight-binding theory. *Physical Review B*, 23(10):5230, 1981.

[22] Walter A Harrison. Theory of the two-center bond. *Physical Review B*, 27(6):3592, 1983.

[23] Lars Hedin. New method for calculating the one-particle green's function with application to the electron-gas problem. *Physical Review*, 139(3A):A796, 1965.

[24] Roald Hoffmann. An extended hückel theory. i. hydrocarbons. *The Journal of Chemical Physics*, 39(6):1397–1412, 1963.

[25] Manu Jaiswal, Candy Haley Yi Xuan Lim, Qiaoliang Bao, Chee Tat Toh, Kian Ping Loh, and Barbaros Ozyilmaz. Controlled hydrogenation of graphene sheets and nanoribbons. *ACS Nano*, 5(2):888–896, 2011.

[26] Hannes Jonsson, Greg Mills, and Karsten W. Jacobsen. Nudged elastic band method for finding minimum energy paths of transitions. *Classical and Quantum Dynamics in Condensed Phase Simulations - Proceedings of the International School of Physics*, pages 385–404, 1998.

[27] Ho Jing Kim and Robert G Parr. Integral hellmann-feynman theorem. *The Journal of Chemical Physics*, 41(9):2892–2897, 1964.

[28] Walter Kohn and Lu Jeu Sham. Self-consistent equations including exchange and correlation effects. *Physical Review*, 140(4A):A1133, 1965.

[29] Pekka Koskinen and Ville Mäkinen. Density-functional tight-binding for beginners. *Computational Materials Science*, 47(1):237–253, 2009.

[30] Emmanuel N Koukaras. Fermis golden rule. *Physics Department, University of Patras*.

[31] Cornelius Lanczos. *The Variational Principles of Mechanics*, volume 4. Courier Corporation, 1970.

[32] ZM Li, ZK Tang, HJ Liu, N Wang, CT Chan, R Saito, S Okada, GD Li, JS Chen, N Nagasawa, et al. Polarized absorption spectra of single-walled 4 $\mathring{A}$ carbon nanotubes aligned in channels of an $AlPO_4$- 5 single crystal. *Physical Review Letters*, 87(12):127401, 2001.

[33] Richard L Liboff. *Introductory Quantum Mechanics*. Addison-Wesley, 2003.

[34] Hongtao Liu, Yunqi Liu, and Daoben Zhu. Chemical doping of graphene. *Journal of Materials Chemistry*, 21(10):3335–3345, 2011.

[35] Chenglin Luo. A transferable tight-binding potential for nickel. *Modelling and Simulation in Materials Science and Engineering*, 6:603–606, 1999.

[36] Satoshi Maeda and Koichi Ohno. A new approach for finding a transition state connecting a reactant and a product without initial guess: Applications of the scaled hypersphere search method to isomerization reactions of HCN, $(H2O)_2$, and alanine dipeptide. *Chemical Physics Letters*, 404(1-3):95–99, 2005.

[37] AG Marinopoulos, Lucia Reining, Angel Rubio, and Nathalie Vast. Optical and loss spectra of carbon nanotubes: Depolarization effects and intertube interactions. *Physical Review Letters*, 91(4):046402, 2003.

[38] Richard M Martin. *Electronic Structure: Basic Theory and Practical Methods*. Cambridge University Press, 2004.

[39] Joseph E. Mayer and Maria Goeppert Mayer. The polarizabilities of ions from spectra. *Phys. Rev.*, 43:605–611, Apr 1933.

[40] JW McClure. Band structure of graphite and de Haas-van Alphen effect. *Physical Review*, 108(3):612, 1957.

[41] Donald JR Meagher. Octree encoding: A new technique for the representation, manipulation and display of arbitrary 3-d objects by computer. *Electrical and Systems Engineering Department Rensseiaer Polytechnic Institute Image Processing Laboratory*, 1980.

[42] Normand Mousseau, Laurent Karim Béland, Peter Brommer, Jean-François Jean-Francois Joly, Fedwa El-Mellouhi, Eduardo Machado-Charry, Mihai-Cosmin Marinica, and Pascal Pochet. The Activation-Relaxation Technique: ART Nouveau and Kinetic ART. *Journal of Atomic, Molecular, and Optical Physics*, 2012:1–14, 2012.

[43] AH Castro Neto, F Guinea, NMR Peres, Kostya S Novoselov, and Andre K Geim. The electronic properties of graphene. *Reviews of Modern Physics*, 81(1):109, 2009.

[44] Kostya S Novoselov, Andre K Geim, SV Morozov, D Jiang, Y_ Zhang, SV Dubonos, IV Grigorieva, and AA Firsov. Electric field effect in atomically thin carbon films. *Science*, 306(5696):666–669, 2004.

[45] Anthony T Paxton. An introduction to the tight binding approximation–implementation by diagonalisation. *Multiscale Simulation Methods in Molecular Sciences*, 42(145-176), 2009.

[46] Valentin N Popov and Luc Henrard. Comparative study of the optical properties of single-walled carbon nanotubes within orthogonal and nonorthogonal tight-binding models. *Physical Review B*, 70(11):115407, 2004.

[47] Dirk Porezag, Th Frauenheim, Th Köhler, Gotthard Seifert, and R Kaschner. Construction of tight-binding-like potentials on the basis of density-functional theory: Application to carbon. *Physical Review B*, 51(19):12947, 1995.

[48] EA Power and T Thirunamachandran. The multipolar hamiltonian in radiation theory. In *Proceedings of the Royal Society of London A: Mathematical, Physical and Engineering Sciences*, volume 372, pages 265–273. The Royal Society, 1980.

[49] Edwin Albert Power and Sigurd Zienau. Coulomb gauge in non-relativistic quantum electro-dynamics and the shape of spectral lines. *Philosophical Transactions of the Royal Society of London A: Mathematical, Physical and Engineering Sciences*, 251(999):427–454, 1959.

[50] EE Salpeter and Hans Albrecht Bethe. A relativistic equation for bound-state problems. *Physical Review*, 84(6):1232, 1951.

[51] Timos Sellis, Nick Roussopoulos, and Christos Faloutsos. The r+-tree: A dynamic index for multi-dimensional objects. *Very Large Data Base Endowment Inc.*, 1987.

[52] T. W. Shattuck. Physical chemistry lecture notes. *Colby College*, 2013.

[53] RN Silver and H Röder. Calculation of densities of states and spectral functions by chebyshev recursion and maximum entropy. *Physical Review E*, 56(4):4822, 1997.

[54] RN Silver, H Roeder, AF Voter, and JD Kress. Kernel polynomial approximations for densities of states and spectral functions. *Journal of Computational Physics*, 124(1):115–130, 1996.

[55] John C Slater. Hellmann-Feynman and virial theorems in the Xα method. *The Journal of Chemical Physics*, 57(6):2389–2396, 1972.

[56] John C Slater and George F Koster. Simplified LCAO method for the periodic potential problem. *Physical Review*, 94(6):1498, 1954.

[57] Patrice E Turchi, Antonios Gonis, and Luciano Colombo. *Tight Binding Approaches to Computational Materials Science*, volume 491. 1998.

[58] Wilfred G van der Wiel, Silvano De Franceschi, Jeroen M Elzerman, Toshimasa Fujisawa, Seigo Tarucha, and Leo P Kouwenhoven. Electron transport through double quantum dots. *Reviews of Modern Physics*, 75(1):1, 2002.

[59] Léon Van Hove. The occurrence of singularities in the elastic frequency distribution of a crystal. *Physical Review*, 89(6):1189, 1953.

[60] Philip Richard Wallace. The band theory of graphite. *Physical Review*, 71(9):622, 1947.

[61] Xuan Wang, Linjie Zhi, and Klaus Müllen. Transparent, conductive graphene electrodes for dye-sensitized solar cells. *Nano Letters*, 8(1):323–327, 2008.

[62] Yang Wang and CH Mak. Transferable tight-binding potential for hydrocarbons. *Chemical Physics Letters*, 235(1):37–46, 1995.

[63] Alexander Weiße and Holger Fehske. Chebyshev expansion techniques. In *Computational Many-particle Physics*, pages 545–577. Springer, 2008.

[64] Alexander Weiße, Gerhard Wellein, Andreas Alvermann, and Holger Fehske. The kernel polynomial method. *Reviews of Modern Physics*, 78(1):275, 2006.

[65] RG Woolley. On the hamiltonian theory of the molecule - electromagnetic field system. *Molecular Physics*, 22(6):1013–1023, 1971.

[66] Jian Zhou, Miao Miao Wu, Xiao Zhou, and Qiang Sun. Tuning electronic and magnetic properties of graphene by surface modification. *Applied Physics Letters*, 95(10):103108, 2009.